March 2017

Dynamical conditions of ice supersaturation and ice nucleation in convective systems: A comparative analysis between in situ aircraft observations and WRF simulations

John D'Alessandro
San Jose State University

Minghui Diao
San Jose State University, minghui.diao@sjsu.edu

Chenglai Wu
University of Wyoming

Xiaohong Liu
University of Wyoming

Ming Chen

See next page for additional authors

Authors

John D'Alessandro, Minghui Diao, Chenglai Wu, Xiaohong Liu, Ming Chen, Hugh Morrison, Trude Eidhammer, Jorgen Jensen, Aaron Bansemer, Mark Zondlo, and Joshua DiGangi

Dynamical conditions of ice supersaturation and ice nucleation in convective systems: a comparative analysis between in-situ aircraft observations and WRF simulations

John J. D'Alessandro[1], Minghui Diao*[1], Chenglai Wu[2,3], Xiaohong Liu[2], Ming Chen[4], Hugh Morrison[4], Trude Eidhammer[5], Jorgen B. Jensen[6], Aaron Bansemer[4], Mark A. Zondlo[7], Josh P. DiGangi[8]

[1]Department of Meteorology and Climate Science, San Jose State University, San Jose, CA, USA, 95192-0104

[2]Department of Atmospheric Science, University of Wyoming, Laramie, WY, USA, 82071.

[3]International Center for Climate and Environment Sciences, Institute of Atmospheric Physics, Chinese Academy of Sciences, Beijing, China, 1000294

[4]Mesoscale & Microscale Meteorology Division, National Center for Atmospheric Research, Boulder, CO, USA, 80301

[5]Research Applications Laboratory, National Center for Atmospheric Research, Boulder, CO, USA, 80301

[6]Research Aviation Facility, National Center for Atmospheric Research, Broomfield, CO, USA, 80021

[7]Department of Civil and Environmental Engineering, Princeton University, Princeton, NJ, USA, 08544

[8]Chemistry and Dynamics Branch, NASA Langley Research Center, Hampton, VA, USA, 23666

***Corresponding author:**

Minghui Diao, Assistant Professor

Department of Meteorology and Climate Science, San Jose State University

One Washington Square, San Jose, CA 95192-0104

Minghui.diao@sjsu.edu; Phone: 609-933-6665

Key points:

Ice supersaturation (ISS) occurrence frequencies in simulations show greater dependence on vertical velocity than observations

Cooper parameterization of ice crystal formation suppresses ISS magnitude and frequency

Model-observation comparison results show improvements by limiting ice nucleation at lower ISS

Abstract

Occurrence frequency and dynamical conditions of ice supersaturation (ISS, where relative humidity with respect to ice (RHi) > 100%) are examined in the upper troposphere around convective activity. Comparisons are conducted between in-situ airborne observations and the Weather Research and Forecasting model simulations using four double-moment microphysical schemes at temperatures ⩽ -40°C.

All four schemes capture both clear-sky and in-cloud ISS conditions. However, the clear-sky (in-cloud) ISS conditions are completely (significantly) limited to the RHi thresholds of the Cooper parameterization. In all of the simulations, ISS occurrence frequencies are higher by ~3–4 orders of magnitude at higher updraft speeds (> 1 m s^{-1}) than those at the lower updraft speeds when ice water content (IWC) > 0.01 g m^{-3}, while observations show smaller differences up to ~1–2 orders of magnitude. The simulated ISS also occurs less frequently at weaker updrafts and downdrafts than observed. These results indicate that the simulations have a greater dependence on stronger updrafts to maintain/generate ISS at higher IWC. At lower IWC (⩽ 0.01 g m^{-3}), simulations unexpectedly show lower ISS frequencies at stronger updrafts. Overall, the Thompson aerosol-aware scheme has the closest magnitudes and frequencies of ISS > 20% to the observations, and the modified Morrison has the closest correlations between ISS frequencies and vertical velocity at higher IWC and number density. The Cooper parameterization often generates excessive ice crystals and therefore suppresses the frequency and magnitude of ISS, indicating that it should be initiated at higher ISS (e.g., ⩾ 25%).

1. Introduction

Cirrus clouds cover approximately 30% of Earth at any given time [*Wylie and Menzel*, 1999], and the global coverage of cirrus clouds plays a critical role in the global radiative budget [*Liou*, 1986; *Chen et al.*, 2000]. The microphysical properties of cirrus clouds play a critical role in their radiative properties. These properties consist of ice particle mass, number concentration, size distributions, as well as particle shape and surface roughness. An important factor that directly affects the initiation of ice crystal formation as well as the microphysical properties is the distribution of relative humidity with respect to ice (RHi).

Ice supersaturation (ISS) occurs when the ambient vapor pressure exceeds the saturation vapor pressure with respect to ice (i.e., ISS = RHi – 100%). The formation of ice clouds requires the ambient conditions to be supersaturated with respect to ice. Unlike warm clouds, which are composed entirely of liquid and develop when a fractional amount of supersaturation with respect to water exists, ice cloud formation will not necessarily take place given the precondition of ISS [e.g., *Heymsfield et al.*, 1998; *Gierens et al.*, 1999; *Spichtinger et al.*, 2003; *Peter et al.*, 2006; *Krämer et al.*, 2009; *Diao et al.*, 2014]. A critical relative humidity is often established to predict the onset of homogeneous nucleation, based on the water activity of the solution [*Koop et al.*, 2000]. Concerning heterogeneous nucleation, ice nuclei (IN) can effectively nucleate ice particles depending on temperature, RHi, and the physical and chemical properties of the IN [*Heymsfield and Miloshevich*, 1995; *Pruppacher and Klett*, 1996; *DeMott et al.*, 2011]. The magnitudes of the ambient RHi can also impact size and number concentrations of ice particles formed via both homogeneous and heterogeneous nucleation.

Anvil cirrus clouds are generally composed entirely of ice and are associated with upper-level outflow during episodes of convective activity. Three factors are often involved in the processes affecting the microphysical properties of anvil cirrus: RHi, the occurrence of pre-existing ice particles, and vertical velocity [*Heymsfield et al.*, 2005]. Vertical velocity is important to consider due to rising (sinking) air associated with temperature decrease (increase) as a consequence of adiabatic expansion (compression). Therefore, an examination of vertical velocity is necessary to correctly characterize temperature fluctuations and cooling/heating rates. A notable positive relationship between updraft speeds and RHi has been reported for some time [*Heymsfield*, 1977]. Previous studies using composite observations at various vertical levels have suggested temperature to be the most important factor in initiating ISS in the upper troposphere, whereas fluctuations of water vapor are of secondary importance [*Kärcher and Haag*, 2004]. More recently, analyses utilizing in-situ flight observations showed that by further restricting the analysis to quasi-isobaric levels, water vapor spatial heterogeneities are the dominant factor that determines the locations and magnitudes of ISS rather than temperature spatial heterogeneities [*Diao et al.*, 2014].

Recently, a study utilizing a box model analyzed the time evolution of ice microphysical properties in relation to various constant background vertical velocities [*Krämer et al.*, 2016].

The study found that modifying the vertical velocities from 0–3 m s^{-1} can significantly impact the evolution of RHi, ice water content (IWC), the effective radius (r_e), and number concentration (Nc) of ice particles, with the resulting IWC, r_e, and Nc varying by several orders of magnitude. Other studies have also investigated the competition between various ice nucleation and freezing modes, and their impacts on properties such RHi, IWC and Nc [e.g., *Gierens*, 2003; *Eidhammer et al.*, 2009; *Barahona and Nenes*, 2009]. Gierens [2003] used a box model and showed that whether heterogeneous or homogeneous freezing dominates is determined by temperature, updraft speed, ambient pressure, and ISS. The author noted that vertical velocity could differentiate whether heterogeneous or homogeneous nucleation would occur, with stronger updrafts (on the order of 0.1 m s^{-1} for pristine conditions to 1 m s^{-1} for polluted conditions) generally associated with homogeneous nucleation. The significance of vertical velocity as a diagnostic parameter for ice microphysical properties, however, is still uncertain. Muhlbauer et al. [2014] analyzed in-situ observations of ice microphysical properties of cirrus clouds formed by various synoptic conditions and found that the probability density functions (PDFs) of vertical velocity perturbations were similar amongst cirrus associated with strong convection (anvil cirrus), frontal lifting around midlatitude cyclones, and upper-level ridges, while particle size distributions were found to have distinct differences associated with these mesoscale or synoptic conditions. Because of this, they concluded that vertical velocity is a poor predictive parameter for ice cloud microphysical properties.

The purpose of this study is to evaluate the frequency and magnitude of the simulated ISS in the upper troposphere in the Weather Research and Forecasting (WRF) model and compare results with in-situ observations. Previously, Diao et al. [2015] examined in-situ airborne observations of RHi in the upper troposphere/lower stratosphere over North America and found the average occurrence frequencies of ISS to be ~1.5–2 times greater on the anticyclonic side of the polar jet stream compared with the cyclonic side. This study aims to similarly examine the occurrence and magnitude of RHi in convective regions. Additionally, the sensitivity of ISS to local cooling rates driven by adiabatic expansion is examined by directly relating ISS to vertical velocity within convective cirrus, anvil cirrus, and surrounding convective systems. Examination of the RHi – vertical velocity relationship at larger spatial scales is certainly warranted; however, the purpose of this study is to examine this relationship at the microscale by comparing in-situ observations and WRF simulations. We will mainly compare the correlations among ISS, vertical velocity, and ice microphysical properties (i.e., IWC and Nc). Sensitivity tests to address whether the compared correlations represent general physical processes or show a strong dependence on spatial/temporal sampling are also discussed. Overall, our comparison results help to evaluate the general performance of various microphysics schemes in the WRF model.

2. Data and methodology

2.1 In-situ measurements

In-situ measurements were taken by the National Science Foundation (NSF)/National Center for Atmospheric Research (NCAR) Gulfstream-V (GV) research aircraft during the NSF Deep Convective Clouds and Chemistry (DC3) campaign. The DC3 campaign took place during May 18 – June 30 2012 at the following locations: northeastern Colorado, northern Alabama, west Texas, and central Oklahoma. The campaign's objective was to target areas of convective outflow in midlatitude regions, with a major focus on observing NO_x production by lightning (Barth et al. [2015] provides a detailed description of the DC3 campaign).

A total of 22 flights were performed by the GV aircraft, each with one-second merged data (~250 m horizontal scale for 1 Hz data) from a suite of instrumentation. Water vapor measurements were taken from the 25 Hz, open-path Vertical Cavity Surface Emitting Laser (VCSEL) hygrometer. Water vapor measurements are averaged to 1 Hz for consistency with other measurements. The accuracy and precision of water vapor measurements are ~6% and ⩽ 1%, respectively. Ice water content (IWC) is derived from the Fast Two-Dimensional Optical Array cloud probe (Fast-2DC), which uses high-speed electronics and a 64-element 25 μm-resolution diode array in order to shadow particles at the sampling speeds of the GV. To reduce uncertainties, only the particles that shadow a minimum of three or more diodes (having a diameter of 62.5 μm or more) are included in the dataset. The effects of shattered ice particles on the exterior arms or inlet shields of cloud probes are potentially important when analyzing airborne ice particle measurements [e.g., *Jensen et al.*, 2009]. The Fast-2DC is equipped with anti-shattering tips to minimize these effects. However, there is no perfect solution to completely eliminate shattering, as previously reported [*Korolev et al.*, 2013]. This study focuses on IWC when evaluating ice particle measurements, which should result in lower uncertainties from ice particle shattering than number concentrations. The IWC is derived from diameter and number concentration measured by Fast-2DC using equations from Brown and Francis [1995]. Temperature measurements were taken by a Rosemount temperature probe with the accuracy and precision of ~±0.3 K and ~0.01 K, respectively. Vertical velocity measurements were derived from a suite of instrumentation, including the Radome Gust Wind Package, pitot tubes, temperature probe, inertial reference unit, and the differential Global Positioning System, which has a precision of ~0.012 m s^{-1} and accuracy of ~0.15 – 0.3 m s^{-1}. According to an in-flight intercomparison conducted by the NCAR Research Aviation Facility between the GV vertical velocity measurements and the NCAR Laser Air Motion Sensor (LAMS) instrument, very good agreement is shown between them. RHi is derived from water vapor mixing ratio, pressure, and temperature following the calculations in Murphy and Koop [2005]. When combining the uncertainties in water vapor and temperature measurements, the uncertainty of RHi for the sampling range of 233.15 K to 207 K is ~6.9%–7.4%.

2.2 WRF simulations

The Advanced Research WRF model simulations (version 3.7) were run with four microphysics schemes, Morrison et al. [2009], a modified Morrison, Thompson et al. [2008], and Thompson and Eidhammer [2014] (hereafter referred to as Morrison, Morrison-125%, Thompson, and Thompson-aerosol, respectively) using the Global Forecast System (GFS) 6-hourly 0.5°×0.5° initialization data. Each simulation has a parent domain (12 km horizontal grid spacing) and a nested domain (2.4 km horizontal grid spacing) with 40 vertical levels and a pressure top of 30 hPa (except for 70 hPa in Thompson-aerosol). Simulations were run starting on 19 May 2012 at UTC 0000 for 30 hours. We also conducted 800 m horizontal grid spacing nested domain simulations for all microphysics schemes and the sensitivity tests show no significant impacts on our conclusions. The timesteps for the parent and two nested domains are 60, 12 and 4 seconds, respectively (except for Thompson-aerosol with 30, 6 and 2 seconds, respectively). Figure 1 A shows the parent and nested domains, as well as the DC3 flight paths. The Kain-Fritsch convective scheme [*Kain*, 2004] was only used in the parent domain. Additionally, the physics options used in both the parent and nested domains of the four simulations were the Dudhia shortwave radiation [*Dudhia,* 1989], the Rapid Radiative Transfer Model (RRTM) longwave radiation [*Mlawer et al.*, 1997], the Noah land surface model [*Chen* *and Dudhia*, 2001], and the Mellor-Yamada-Janjic planetary boundary layer scheme [*Janjić*, 1994].

Both Morrison and Thompson include number concentrations of newly formed ice crystals predicted by the Cooper [1986] parameterization, which is solely a prognostic function of temperature, $\mathrm{Nc_i} = 0.005\exp[0.304 * (\mathrm{T_0} - \mathrm{T})]$, where $\mathrm{Nc_i}$ is the number of ice crystals initiated ($\mathrm{L^{-1}}$), $\mathrm{T_0}$ is 273.15 K, and T is the ambient temperature in Kelvin. Morrison and Thompson initiate the Cooper parameterization when RHi exceeds 108% and 125% (or when liquid saturation is reached below 265.15 K and 261.15 K), respectively, while Thompson-aerosol does not include the Cooper parameterization. The only modification in Morrison-125% is to increase the RHi threshold for initiating the Cooper parameterization from the default value (RHi of 108%) to RHi of 125%. Additional restrictions on the Cooper parameterization are applied, for example, Morrison and Thompson restrict the number concentration of ice particles formed via the Cooper parameterization to 500 $\mathrm{L^{-1}}$ and 250 $\mathrm{L^{-1}}$, respectively, and the mass-weighted mean size of cloud ice may not exceed 300 μm in Thompson. Both Morrison and Thompson also allow for homogeneous and heterogeneous freezing of cloud droplets and rain, where heterogeneous freezing is parameterized following Bigg [1953] (for both schemes) and homogeneous freezing occurs instantaneously at -40°C and -38°C, respectively. Frozen cloud droplets and rain can potentially account for a significant portion of the total Nc of frozen hydrometeors in and around convection systems, where liquid droplets can be lofted to the homogeneous freezing level. The treatment of deposition/sublimation rates for ice and snow in Morrison is similar to Harrington et al. [1995], Ferrier [1994] and Reisner et al. [1998], whereas the calculations in Thompson are based on Srivastava and Coen [1992].

Thompson-aerosol is similar to Thompson, but explicitly treats aerosols categorized as either "water friendly" (hygroscopic) or "ice friendly" (non-hygroscopic), allowing for the activation of aerosols as both IN and cloud condensation nuclei, initialized with the climatological aerosol dataset. As described in Thompson and Eidhammer [2014], deposition freezing (below water saturation) is parameterized with Phillips et al. [2008], while immersion freezing (at or above water saturation) is now parameterized with DeMott et al. [2011]. Homogeneous nucleation of the "water friendly" aerosols is parameterized with Koop et al. [2000]. At the temperatures considered in this study (≤ -40°C), the DeMott parameterization will not activate since homogeneous nucleation initiates at lower RHi compared with the DeMott parameterization. Thus, while the Cooper parameterization in the other three microphysics schemes implicitly includes heterogeneous and homogeneous nucleation, Thompson-aerosol allows for explicit simulations of the competition between heterogeneous and homogenous nucleation.

All four microphysics schemes allow for supersaturation with respect to ice, without applying the saturation adjustment to the ice hydrometeors. In addition, all microphysics schemes calculate the saturation vapor pressure with respect to ice following Flatau et al. [1992]. Differences in the calculated RHi between Murphy and Koop [2005] and Flatau et al. [1992] are minimal, ranging from ~0% to 0.34% at the combined water vapor and temperature ranges sampled by the DC3 observations at -40°C and -65.8°C. However, there are somewhat larger differences in liquid saturation between Flatau et al. [1992] and Murphy and Koop [2005], so that slightly higher RHi values of 1.17% – 15.75% and 1.14% – 6.42% occur at liquid saturation in both the Thompson and Morrison simulations based on Flatau et al. [1992] compared to Murphy and Koop [2005]. This explains the occurrence of a small number of points in the simulations with RHi exceeding the liquid saturation line calculated by Murphy and Koop [2005].

Our main analyses are based on simulations over the Great Plains region on 19 May 2012, during a convective episode throughout the area. The event was marked by several high wind (> 33 m s^{-1}) and hail (diameter > 5 centimeters) reports stretching from Southern OK up to Western IA. The GV took observations on this day over Oklahoma, where a squall line associated with the high winds and large hail occurred. The event was marked by elevated instability and widespread values of CAPE above 1000 J kg^{-1} throughout most of the region. A composite dataset for each simulation is obtained by combining outputs at four times, UTC 1800, 2100, 0000, and 0300 from 19–20 May 2012 (i.e., 1–10 pm local time on 19 May 2012). These outputs are chosen from the simulations to obtain data sampled over nine hours of a convective episode, which included multiple clusters of thunderstorms and a well-developed squall line in the southern domain (see Figure 1 B). High water vapor concentrations from the WRF simulations were found to have similar spatial distributions to those seen in the GOES-13 satellite imagery. Sensitivity tests of another set of realistic case simulations (11–12 June 2012) are also examined, which show consistent conclusions for the statistical distributions of ISS and its correlation with vertical velocity.

To visualize the RHi and vertical velocity (w) fields from the simulations, Figure 1 B–D shows RHi and w spatial distributions for the entire nested domain using Thompson. At 300 hPa, gravity waves are seen surrounding the strongest updrafts and downdrafts, and ISS is often collocated with relatively high fluctuations in w (e.g., between 100°W–95°W) (Figure 1 B). The vertical cross-section view at 40°N (Figure 1 C and D) reveals a deep convective structure with w of ±5 m s^{-1} extending from 875 hPa to 250 hPa. The higher RHi (e.g., > 140%) appears to occur almost exclusively at the upper tropospheric levels within regions of strong updrafts, while weaker updrafts (e.g., w > 0.5 m s^{-1} at 97°W near 300 hPa) also collocate with RHi > 130%.

2.3 Composite datasets for the comparisons between observations and simulations

To conduct the comparison, similar restrictions are imposed on the composite datasets for in-situ observations (1 Hz data from 22 flights) and WRF simulations (all grid points in the nested domain for four time outputs). Data analyses are restricted to regions where the temperature is less than or equal to -40°C to prevent the sampling of mixed-phase clouds for the purposes of solely analyzing the distributions of RHi and microphysical properties of ice particles. The minimum IWC reported for one particle per 1 Hz measurements from the Fast-2DC probe in the DC3 campaign is used to define in-cloud conditions in both observations and simulations (i.e., IWC $\geqslant 3.82\times10^{-5}$ g m^{-3}), whereas clear-sky conditions are defined when IWC is less than this threshold. The four microphysics schemes considered in this study predict mass mixing ratios for three types of frozen hydrometeors: ice, snow, and graupel. For the simulations, IWC is treated as the sum of these quantities. Similarly, Nc is treated as the total number of the frozen hydrometeors. Morrison and Morrison-125% predict Nc for ice, snow, and graupel, whereas Thompson and Thompson-aerosol only predict Nc for ice. The observational data are restricted to below the tropopause, where the tropopause height is based on the National Centers for Environmental Prediction (NCEP) GFS-FNL (final) dataset interpolated onto the GV aircraft position and time. Simulation datasets are restricted to regions where ambient pressure $\geqslant$ 148 hPa (i.e., the lowest pressure sampled by GV in DC3). With these restrictions imposed, the total number of 1 Hz observations in 22 flights amounts to ~67 hr, compared with ~10^6 of grid points in the 2.4 km nested domain for four time outputs. We also examined the correlations between

ISS probabilities and w by using the in-situ observations onboard the NASA DC8 research aircraft during the DC3 campaign, and found consistent correlations between ISS frequencies and w as those shown in the composite dataset from the GV aircraft.

3. Results

3.1 RHi distributions at various temperatures for clear-sky and in-cloud conditions

Occurrences of RHi are shown for both in-cloud and clear-sky conditions (Figure 2 left two columns). Throughout the entire temperature distribution shown for the observations, RHi ranges from ~10% to as high as 160% and 150% for in-cloud and clear-sky conditions, respectively. The few occurrences of RHi above the liquid saturation line are within the range of measurement uncertainties. Similar to the observations, the simulated in-cloud RHi most frequently occur within ±5% to ±15% of ice saturation, yet they all extend to higher values (RHi around 180%) compared with the observations. Additionally, all of the simulations show a slight increase in RHi occurrences around the liquid saturation line, which may be attributed to regions near and within the convective core of deep convective systems (as illustrated in Figure 1 B–D), where aircraft would avoid sampling due to strong turbulence. Previously, simulations of an idealized squall line scenario without synoptic scale dynamic forcings and radiative forcings did not capture ISS at clear-sky conditions [*Diao et al.*, submitted]. Thus, the capability of capturing ISS at both clear-sky and in-cloud conditions in the WRF simulations suggests that larger-scale dynamical forcings and/or radiative forcings play an important role in ISS formation.

The unrealistic limits of the clear-sky RHi magnitudes in Morrison, Morrison-125% and Thompson are also the respective RHi thresholds for initiating the Cooper parameterization (i.e., RHi of 108%, 125%, and 125%, respectively). Similarly, sharp gradients are seen for in-cloud RHi distributions. In comparison, Thompson-aerosol without the Cooper parameterization shows clear-sky ISS extending to the liquid saturation line, with ISS as high as ~60% occurring at colder temperatures. By increasing the default threshold of initiating the Cooper parameterization, Morrison-125% produces more comparable results to the observations than the default Morrison in terms of the magnitude and frequency of ISS allowed at the relatively higher RHi (> 108%).

The PDFs of RHi are compared among observations and four individual WRF time outputs (Figure 2 right two columns). For in-cloud conditions, the PDF of RHi for DC3 dataset centers at ~100%, which is consistent with previous in-situ observations of in-cloud RHi distributions [*Ovarlez et al.*, 2002; *Krämer et al.*, 2009; *Diao et al.*, 2014]. Morrison, Thompson and Thompson-aerosol all have much higher in-cloud RHi probabilities (~0.16 – 0.18) centered at ice saturation compared with that of observations (~0.09), while Morrison-125% has the most comparable RHi frequency (~0.1) at ice saturation. The variations in RHi distributions with respect to different time outputs appear minimal for the simulations, where the most notable change are the narrower peaks of PDF centered at RHi = 100% along the time evolution. Thompson-aerosol is the only scheme that allows for noticeable RHi probabilities at RHi > 125% as seen in the observations, especially for the earlier time outputs, even though this scheme shows slightly higher probabilities (e.g., ~0.01–0.02 at RHi = 130%) at this RHi range than those in the observations (~0.01 at RHi = 130%).

For clear-sky conditions, PDFs of RHi for the simulations and observations both peak around 10%. However, the decay of RHi frequency from RHi of 20% to 80% is much sharper in all the simulations, while the RHi frequency appears almost constant from 40%–80% in the observations. In addition, observations show higher probabilities of clear-sky ISS than simulations, with Thompson-aerosol having the highest clear-sky ISS frequency amongst the simulations. These discrepancies between observations and simulations may be subject to sampling differences between DC3 and WRF, since the GV aircraft often sampled regions within 24 hours of convective activity, whereas the entire nested domain of WRF simulations is included in the datasets (as shown in Figure 1). However, we note that the lack of clear-sky ISS occurrence frequencies in the simulations is not necessarily due to a lack of clear-sky sampling. In fact, the total number of samples (i.e. 1 Hz data and grid points) for in-cloud and clear-sky conditions are proportionally about 1:2 in DC3 and about 1:7 in the WRF simulations.

3.2 Temperature, vertical velocity, IWC, and Nc distributions inside ISS conditions

The normalized frequency distributions of temperature, w, IWC and Nc are shown for various ranges of ISS (Figure 3 A–D and E–H). Temperature distributions of the four simulations are similarly well dispersed, whereas observations sampled more frequently at -50°C to -46°C than at -46°C to -40°C.

The PDFs of w for in-cloud (clear-sky) ISS conditions (Figure 3 C and D) are centered at 0.34 m s^{-1} (-0.02 m s^{-1}) and ~0.14 m s^{-1} (~0.01 m s^{-1}) for observations and simulations, respectively, showing a slightly higher average w for in-cloud ISS in the observations. The cumulative frequency distributions (CFDs) of w for in-cloud ISS (Figure 3 E) show strong sensitivities to ISS magnitudes in Morrison and Morrison-125%, with their 90th percentile of w increases from 0.25 m s^{-1} to 1–2 m s^{-1} when ISS increases from below to above 20% (Figure 3 E). For clear-sky conditions, the CFDs of w are similar between the observations and simulations for different ISS ranges (> 20% and < 20%) (Figure 3 F). This suggests that vertical velocity, as a parameter, may be a poor predictor for the magnitude of clear-sky ISS. Standard deviations of ~0.9 m s^{-1} are seen for all the simulations compared to ~0.57 m s^{-1} in the observations as a result of the intense updrafts and downdrafts sampled in simulations (up to ~50 m s^{-1} in Morrison and Morrison-125%, ~40 m s^{-1} in Thompson and Thompson-aerosol, and as low as ~ -17 m s^{-1} in all the simulations).

Large differences in IWC and Nc distributions exist among the observations and simulations for different ranges of ISS. In Morrison, the IWC distribution peaks at ~0.025 g m^{-3} for ISS $\leqslant$ 20%, and this peak shifts to a significantly larger value at ~2.5 g m^{-3} for ISS > 20%, which is ~1.5 orders of magnitude greater than that in the observations (Figure 3 G). Thompson-aerosol has the opposite trend compared with Morrison, as it shows a decreasing IWC trend with increasing ISS magnitudes. In addition, the average Nc in Thompson-aerosol decreases by more than a factor of 4 from ISS $\leqslant$ 20% to ISS > 20%. In fact, Thompson-aerosol is the only scheme that shows both decreasing IWC and Nc with increasing ISS, similar to the observations.

Consequences of the different IWC and Nc distributions among the various simulations can be seen in the CFDs of w for in-cloud ISS conditions. When higher IWC and/or Nc exist, higher w are often seen to be associated with in-cloud ISS conditions. For in-cloud ISS > 20%, Morrison and Thompson-aerosol have ~20% and 80% of w below 0.25 m s^{-1}, respectively, likely due to the higher IWC and Nc values in Morrison. These results are consistent with the previous theoretical calculations, which showed that ice cloud properties can significantly impact the in-cloud ISS distributions due to the depositional growth of ice crystals [Kärcher 2012]. Thus, it is crucial to account for in-cloud properties (e.g., IWC and Nc) when evaluating the impacts of various magnitudes of vertical velocity on the characteristics of ISS.

3.3 Average vertical velocities for in-cloud ISS conditions

Analysis of average w for in-cloud conditions associated with various magnitudes of ISS is shown in Figure 4. The factors of IWC and Nc are separately accounted for (on the y-axis of Figure 4) in order to appropriately evaluate the impacts of various magnitudes of w on ISS. The average w is calculated within each bin of log-scale IWC (or Nc) for various ranges of ISS. To examine the potential effects of ice shattering artifacts in the observational dataset, additional analysis excluding ice particles smaller than 100 μm is shown (Figure 4, panel A3), which is consistent with the observations including particles ⩾ 62.5 μm (panel A2). We note that since the simulations include all frozen hydrometeors extending to size of zero, the Nc in observations would have a low bias due to the lack of small particles, while the IWC comparisons dominated by larger particles would be less affected.

For observations, the average w increases with the increasing IWC and Nc when they exceed 0.001 g m^{-3} and 1 L^{-1}, respectively. Such increases in the average w with IWC or Nc become even greater as the magnitudes of ISS increase. For simulations, at IWC > 0.01 g m^{-3} or Nc > 100 L^{-1}, the differences in the average w for the various magnitudes of ISS are much larger (i.e., by ~1–15 m s^{-1}) than those in the observations (by ~0.2–1 m s^{-1}). Thus, both observations and simulations show that on average the presence of higher updrafts are required to initiate/maintain the higher magnitudes of in-cloud ISS when associated with relatively high IWC (or Nc), yet the average w in simulations is even higher at the same magnitudes of in-cloud ISS. Note that the Morrison simulation does not have IWC < 10^{-3} g m^{-3} or Nc < 300 L^{-1} at RHi ⩾ 108%, due to the initiation of ice crystal formation from the Cooper parameterization. In addition, as the only scheme that does not include the Cooper parameterization, Thompson-aerosol is the only simulation that captures the low values of IWC (i.e., ~3×10^{-5} g m^{-3}) and Nc (~0.01 L^{-1}) for each interval of ISS shown.

3.4 Correlations between the probabilities of ISS and w for in-cloud conditions

To examine the physical processes controlling ISS formation in the WRF simulations, we compare the simulated correlations between ISS probabilities and w with those from observations for in-cloud conditions (Figures 5 and 6). The comparisons between observations and simulations in Figures 5 and 6 are restricted to the same ranges of w, which exclude the extreme updrafts and downdrafts sampled in the simulations but not in the observations as discussed prior (Figure 3). By restricting the analysis to the same ranges of w, we avoid sampling biases in w for the comparisons. Probabilities of ISS are calculated for each given range of w, that is, the number of occurrences of ISS (within a given 10% interval) are normalized by the total number of occurrences at all RHi ranges for the given range of w. We also control the factors of IWC and Nc because of their potential influences on ISS characteristics. That is, the ISS probabilities are calculated for various scales of w within individual bins of IWC (Figure 5) and Nc (Figure 6).

For the correlations between ISS probabilities and w, observations show that the probabilities of ISS < 10% are relatively similar for various ranges of w given the same ranges of IWC or Nc (except for a few larger IWC and Nc values). In contrast, all the simulations show decreasing probabilities of ISS < 10% correlated with increasing w. For the higher ISS ⩾ 10%, observations show higher ISS probabilities in the stronger updrafts than weaker updrafts or downdrafts. The increases in ISS probabilities from weaker to stronger updrafts are even more evident as IWC (or Nc) increases, indicating that stronger updrafts are generally required to generate/maintain ISS when associated with higher IWC or Nc.

Compared with a consistent positive correlation between probabilities of ISS ⩾ 10% and w as shown in the observations, simulations show different correlations between IWC > 0.01 g m^{-3} and IWC ⩽ 0.01 g m^{-3} (Figure 5). Note that Morrison does not have the lower IWC (< 0.01 g m^{-3}) and lower Nc (< 300 L^{-1}) at RHi > 108% due to the excess ice crystal formation from the Cooper parameterization. At IWC > 0.01 g m^{-3}, the main difference between the observations and the other three simulations (Morrison-125%, Thompson, and Thompson-aerosol) is that the simulations show much higher probabilities of ISS associated with relatively strong updrafts than those with weak updrafts or downdrafts. In fact, the differences in the probabilities of ISS ⩾ 10% increase by 1–1.5 orders of magnitude from downdrafts and weaker updrafts to stronger updrafts in the observations, while those in the simulations increase by 2–4 orders of magnitude. Sensitivity tests on individual flights show consistent results where observations have smaller differences in the probabilities of ISS between lower and higher w than the simulations.

Among the four simulations, Morrison-125% has minimal differences in ISS probabilities between higher and lower w below the RHi threshold of initiating the Cooper parameterization. Such improvement in Morrison-125% cannot be accounted for by only adjusting the Nc upper limit in the scheme (the maximum-allowed concentration of ice). This is seen in Figure 5 row 3 with an additional simulation that changes this limit in the Morrison scheme (Nc < 500 L^{-1}) to the value used in Thompson (Nc < 250 L^{-1}), while using the default RHi threshold of 108% (named as Morrison-Nc250). At IWC ≤ 0.01 g m^{-3}, simulations show that probabilities of ISS ≥ 10% are surprisingly lower at relatively higher w (w > 0.5 m s^{-1}) than those at the lower w, by ~0.5–1 orders of magnitude. These results indicate that compared with observations, simulations have a greater dependence on stronger updrafts for generating and/or maintaining ISS ⩾ 10% at the higher IWC values, while an opposite correlation between ISS probabilities and w are shown in the simulations at the lower IWC values. A simulation with twice the number of vertical levels (i.e., 80 levels) was conducted for the Thompson-aerosol scheme (named as Thom-aer-80lev), showing that the differences in the probabilities of ISS > 10% between lower and higher w are still ~2–4 orders of magnitude. In addition, a slight increase in the probabilities of ISS in downdrafts and weaker updrafts by ~0.5 order of magnitude is seen at relatively higher IWC and Nc, suggesting that increasing the number of vertical levels allows for more ISS at lower w for in-cloud conditions.

Compared with the analysis controlling for IWC (Figure 5), the analysis controlling for Nc (Figure 6) shows smaller differences in ISS probabilities by 1–2 orders of magnitude between the higher and lower w in all of the simulations, which are comparable to the scales shown in the observations. Morrison-125% has increasing probabilities of ISS with increasing Nc for almost all ranges of w, while Thompson, Thompson-aerosol, and Thom-aer-80lev show decreasing ISS probabilities at higher Nc. Thom-aer-80lev has the most comparable results to the observed range of ISS probabilities among all of the simulations when controlling for Nc.

Higher resolution WRF simulations using the 800 m nested domain are further examined to evaluate the sensitivities of the simulated correlations between ISS probabilities and w to horizontal grid spacings (Figures 7 and 8). The overall correlations between ISS and w are consistent between the 2.4 km and 800 m horizontal grid spacing simulations, that is, the positive and negative correlations between ISS probabilities and w are consistently shown at IWC > 0.01

g m^{-3} and IWC ⩽ 0.01 g m^{-3}, respectively. The differences between the two resolutions are mainly shown in the differences of ISS probabilities between higher and lower w. Compared with the 2.4 km simulations, the differences of the probabilities of ISS ⩾ 10% in the 800 m simulations decrease (i.e., closer to observations) at higher IWC (> 0.01 g m^{-3}) or Nc (> 10 L^{-1}), but increase (i.e., more dissimilar to observations) at the lower IWC and Nc. These results suggest that increasing the model resolution does not necessarily produce more comparable results to the observations for all IWC and Nc ranges.

3.5 The normalized occurrence frequency of ISS at the full range of w in observations and simulations

When comparing w at the same magnitudes sampled in observations and simulations in Figures 5–8, the full range of w sampled in WRF simulations is not shown. To provide a depiction of the full range of w for in-cloud conditions, the normalized occurrence frequencies of ISS are further analyzed in relation to all w values, with the factors of IWC and Nc controlled in Figures 9 and 10, respectively. The normalized ISS frequencies are calculated by normalizing the number of ISS data in each IWC–w bin (or Nc–w bin) with the total number of RHi data in that bin, and results are shown in four ranges of ISS from 0–10%, 10%–20%, 20%–30% to ⩾ 30%.

In Figure 9, both observations and WRF simulations show increasing occurrence frequencies of ISS at higher updraft speeds and larger IWC, and the higher ISS frequencies in stronger updrafts are more prominent in the simulations than in the observations at IWC > 0.01 g m^{-3}, which is consistent with the comparisons in Figures 5 and 7. At this IWC range, all the simulations show larger increases in the frequencies of ISS ⩾ 20% from near zero to ~0.3 as w increases from 0 to 3 m s^{-1}, while the observations show smaller increases in ISS frequencies (from ~0.1 to ~0.2). In addition, when w is above 3 m s^{-1}, all of the simulations show larger frequencies of ISS ⩾ 20% than those in the observations, while they also show lower ISS frequencies in weaker updrafts and downdrafts (w < 0.5 m s^{-1}). For weaker updrafts and downdrafts, most of the simulated ISS is below 10% (Figure 9 first column), while only Morrison and Morrison-125% allow ISS ⩾ 10% in strong downdrafts (w < -2 m s^{-1}). Thompson-aerosol is the only scheme that shows ISS frequencies greater than 0.1 at the lower IWC (< 0.01

g m^{-3}), since more ice crystals with higher IWC are likely generated due to the Cooper parameterization in the other schemes.

Simulations also show stronger correlations between ISS and Nc than observations at Nc > 100 L^{-1} (Figure 10), which is similar to those shown at IWC > 0.01 g m^{-3}. In addition, a lack of ISS occurrences at w < 0.5 m s^{-1} is shown in all the simulations at ISS $\geqslant$ 10%, except for Morrison-125%. One feature that is shown in Figure 10 but not in Figure 9 is that Thompson-aerosol has a peak ISS frequency at Nc around 0.1 L^{-1}, likely due to the predicted heterogeneous IN number concentration by the Phillips et al. [2008] parameterization. For the same purpose of addressing the effects of potential ice particle shattering as discussed in Figure 4, results with restricted Nc values (excluding ice particles smaller than 100 μm) are also provided. Similar occurrence frequency distributions of ISS are shown in the observations with or without such restriction.

3.6 Examining the influences of different sampling methods, time outputs, and different case studies

To examine the sensitivity of the relationship between ISS and w to the spatial/temporal sampling method, we analyze the normalized occurrence frequencies of ISS for the WRF gridded data collocated with the observations during the May 19th flight (Figure 11 top three rows). WRF gridded data were selected within certain spatial ranges of the in-situ observations in latitude and longitude (i.e., ±0.5°, ±1.5°, and ±3.0°) and within a time window (±30 min). Six hourly outputs were used for the collocated comparisons from May 19th, UTC 2100 to May 20th, UTC 0200. The results are shown for the Thompson-aerosol aware simulation, while other microphysics schemes show similar consistency when conducting the collocated comparisons. In addition, to examine whether the correlations between ISS and w vary with the time evolution of the convective system as well as with different convective events, the normalized occurrence frequencies of ISS are analyzed for three combined time outputs during a separate convective episode on 11–12 June 2012 (Figure 11 bottom four rows). The domain of the 11–12 June 2012 simulations also coincided with flight observations during the DC3 campaign. This day was marked by isolated thunderstorms over Missouri/Arkansas and a mesoscale convective system over Alabama, both of which were sampled by the GV aircraft.

Overall, the two main differences between observations and simulations that are shown in the 19–20 May 2012 case (Figure 9) are also captured in these two sensitivity tests shown in Figure 11, that is, (1) a stronger gradient in ISS frequencies is shown in the simulations than observations at IWC > 0.01 g m^{-3}, and (2) a lack of ISS occurrences at w < 0.5 m s^{-1} is shown in the simulations. In addition, Thompson-aerosol is still the only scheme that captures the ISS frequencies > 0.1 associated with lower IWC values (< 0.01 g m^{-3}) in the 11–12 June 2012 case, even though it shows higher occurrence frequencies of ISS ⩾ 30% at w > 1 m s^{-1} than that in the 19–20 May 2012 case. These results indicate that the comparisons between observations and simulations on the correlations between ISS occurrence frequencies and w do not vary significantly by convective events arising from different synoptic/mesoscale forcings or by using more restrictive sampling methods.

The normalized frequency distributions of ISS are further compared among different time outputs of the same convective episode. Analyses on the four individual time outputs used in the composite datasets of the 19–20 May 2012 case are shown for Morrison and Thompson (Figure 12). There is a noticeable evolution of the normalized frequencies of ISS from UTC 1800 to UTC 0300, namely, the full range of w distributions increases from ± 1 m s^{-1} to greater than ± 6 m s^{-1} at ISS conditions. Nevertheless, the sharp gradient in ISS frequencies between stronger updrafts (w > 0.5 m s^{-1}) and weaker updrafts are still visible amongst individual time steps. In addition, the lack of ISS associated with w < 0.5 m s^{-1} at high IWC values (> 0.01 g m^{-3}) is also consistently shown in these time outputs. These results indicate that even though the range of w varies among different time outputs, the overall distributions of ISS frequencies, as well as their correlations with w and IWC, are consistent regardless of the selection of time outputs for our analysis.

4. Discussions and conclusions

WRF simulations with the Morrison et al. [2009], modified Morrison, Thompson et al. [2008], and Thompson and Eidhammer [2014] microphysics schemes captured both in-cloud and clear-sky ISS. The Cooper parameterization for ice crystal formation is included in the first three schemes but not in Thompson-aerosol. Including or excluding the Cooper parameterization, as well as changing the RHi thresholds for initiating the Cooper parameterization, have large impacts on our analysis of RHi, IWC, and Nc. For RHi distributions at temperature ⩽ -40° C

(Figure 2), Cooper parameterization restricts the frequency and magnitude of ISS in simulations compared with the observations, which is likely due to the high number concentrations of ice particles being formed through this parameterization. By increasing the RHi threshold for the Cooper parameterization from the default 108% to 125% in Morrison-125%, a significant increase in the occurrences of RHi above 108% is shown. Additionally, the Cooper parameterization restricts the simulations from having lower IWC or lower Nc values at larger values of ISS. For example, Morrison does not have IWC < 0.01 g m^{-3} or Nc < 100 L^{-1} at ISS ⩾ 8%. Other microphysics schemes that predict ice nucleation as a function of temperature may potentially yield similar discrepancies as produced via the Cooper parameterization. Thus, results from this study suggest that the Cooper parametrization, if included, should be initiated at higher RHi values (such as RHi ⩾ 125%) at temperatures ⩽ -40°C. Given the simplicity of the Cooper parameterization for more economical computations, adjusting the RHi threshold is found to be most effective for improving the simulations of ISS and ice nucleation compared with modifying other factors (e.g., Nc upper-limit, number of ice nuclei and vapor deposition rate) in both the current study and another study [*Diao et al.*, submitted]. Thus, the Cooper parameterization with the adjustments recommended will still be valuable, and it does not involve the uncertainties of aerosol fields when using the Thompson-aerosol scheme. Based on these results, microphysics schemes are recommended to consider limiting ice nucleation at lower ISS even at low temperatures ⩽ -40°C. These results are consistent with the previous remote sensing studies focusing on warmer conditions (> -40°C) suggesting that ice nucleation is limited when RHi is below water saturation [*Ansmann et al.*, 2008; *de Boer et al.*, 2011].

Concerning correlations between ISS and w at various IWC (Nc) ranges, observations show a consistent positive correlation between probabilities of ISS and w (Figures 5 and 6), suggesting that higher w is generally required to generate and/or maintain the higher magnitudes of ISS. Such positive correlations between ISS probabilities and w are stronger when IWC or Nc increases, or when ISS magnitudes increase. In contrast, two types of ISS – w correlations occur in the simulations: a positive correlation at IWC > 0.01 g m^{-3} (or Nc > 100 L^{-1}) and a negative correlation at lower IWC (or lower Nc). Although the simulations have a positive correlation between ISS probabilities and w at higher values of IWC or Nc, such correlations are much stronger in the simulations with differences in ISS probabilities up to 4 orders of magnitudes between weak and strong updrafts (i.e., 0.1 – 4 m s^{-1}). In comparison, the differences in observations are only up to 2 orders of magnitude. The stronger dependence of ISS probabilities on w in the simulations for generating and/or maintaining ISS at IWC > 0.01 g m^{-3} or Nc > 100 L^{-1} is consistently shown in a series of analyses (Figures 5 – 8), and is also evident by the large increases of ISS frequencies from weaker to stronger updrafts in Figures 9 – 12. As a result of this strong dependence on w in the simulations, a lack of ISS is associated with weaker updrafts and downdrafts (w < 0.5 m s^{-1}) at high IWC and Nc values in Figures 9 – 12.

The discrepancies in the correlations between ISS probabilities and w between the observations and WRF simulations may be due to several factors. For in-cloud ISS, it is possible that the relaxation rate of ISS (i.e., the time for the existing ice to deplete the available water vapor over ice saturation) may be excessive at higher IWC (or Nc), which would require stronger updrafts to enhance the magnitudes of RHi as the excess water vapor is rapidly depleted at relatively high IWC (or Nc). A series of previous studies have discussed the complex factors influencing the vapor deposition rates, including studies on the spherical particles [*Korolev and Mazin*, 2003] and the non-spherical particles [*Sheridan et al.*, 2009], as well as those on the uncertainties with regard to the kinetically-limited growth [e.g., *Harrington et al.*, 2009; *Zhang and Harrington*, 2015]. In addition, all the microphysics schemes in this study include homogeneous (and heterogeneous) freezing of cloud droplets and rain, which can affect ice concentrations and ISS relaxation time below -40°C, especially in and near deep convection. Thus, it is not just the representations of ice nucleation on aerosols (as opposed to activated cloud droplets/rain) that can lead to differences between simulations and observations, although large impacts are still seen in the ISS frequency and magnitude when modifying the Cooper parameterization threshold in Morrison-125%.

Another potential explanation for the different ISS – w correlations between the observations and simulations may be that the water vapor spatial heterogeneities on the cloud scale (~1 km) are not sufficiently resolved by the simulations. Water vapor spatial variabilities have been previously reported to be the dominant contributor to the variabilities of RHi for both clear-sky and in-cloud conditions compared with the spatial variabilities of temperature [*Diao et al.*, 2014]. One may argue that increasing the horizontal resolution of the WRF simulations would provide a better representation of the water vapor spatial heterogeneities. However, when reducing the horizontal grid spacing from 2.4 to 0.8 km, even though the ISS probabilities at various w ranges in all the simulations become closer to the observations at IWC > 0.01 g m^{-3} (or Nc > 100 L^{-1}), the simulations also show larger discrepancies compared with the observations for representing ISS probabilities at the lower ranges of IWC and Nc. More investigation, such as using a cloud-resolving model [e.g., *Diao et al.*, submitted], is needed to examine if higher resolution simulations could help to produce more comparable results to the observations.

We caution that there are several caveats with the current analysis, mainly due to various factors in addition to IWC and Nc that potentially influence ISS distributions, such as the evolution of ISS and ice crystal regions [*Diao et al.*, 2013]. The analysis of ISS, IWC, and Nc in this study represents a composite dataset that sampled cirrus clouds at various evolution stages (e.g., nucleation, growth, sedimentation). We examined the correlations between ISS frequencies and w at various pressures and altitudes, and found that these two factors have smaller impacts than those of IWC and Nc. Another potential impact on the formation of ISS is from the various scales of dynamical processes, including smaller scale gravity waves and turbulence, and mesoscale to synoptic scale dynamical conditions, such as frontal uplifting, mesoscale gravity waves, warm conveyor belts, and jet streams [*Spichtinger et al.*, 2005a, 2005b; *Muhlbauer et al.*, 2014; *Diao et al.*, 2015]. Additional work is recommended to further distinguish how the relationship between ISS and vertical velocity is represented by different cloud microphysics schemes in global climate models, where vertical velocity fluctuations associated with mesoscale phenomenon are parameterized due to the sub-grid scale (< 100 km) nature of these fluctuations, as well as in smaller scale model simulations such as the WRF-Large Eddy Simulations.

Acknowledgement

M. Diao acknowledges the funding support of the National Center for Atmospheric Research (NCAR) Advanced Study Program (ASP) Faculty Fellowship in 2016. NCAR is sponsored by the National Science Foundation. J. D'Alessandro acknowledges the support of the Walker Graduate Fellowship from San Jose State University. X. Liu and C. Wu acknowledge support of the U.S. Department of Energy's Atmospheric System Research Program (grant DE-SC0014239). For in-situ observations onboard the NSF GV research aircraft during the DC3 campaign, the VCSEL hygrometer QC/QA is conducted by Josh DiGangi, Minghui Diao, Mark Zondlo and Stuart Beaton; the Fast-2DC probe QC/QA is conducted by Aaron Bansemer; the Rosemount temperature probe and vertical velocity measurements QC/QA are conducted by William Cooper and Jorgen Jensen. We thank the pilots and flight crew at the NCAR Research Aviation Facility for field support. The NSF DC3 dataset is publically available and can be accessed at http://data.eol.ucar.edu/master_list/?project=DC3.

References:

Ansmann, A. et al. (2008), Influence of Saharan dust on cloud glaciation in southern Morocco during the Saharan Mineral Dust Experiment, *J. Geophys. Res.*, *113*(D4), D04210, doi:10.1029/2007JD008785.

Barahona, D., and A. Nenes (2009), Parameterizing the competition between homogeneous and heterogeneous freezing in ice cloud formation – polydisperse ice nuclei, *Atmos. Chem. Phys. Discuss.*, *9*(3), 10957–11004, doi:10.5194/acpd-9-10957-2009.

Barth, M. C. et al. (2015), The Deep Convective Clouds and Chemistry (DC3) Field Campaign, *Bull. Am. Meteorol. Soc.*, *96*(8), 1281–1309, doi:10.1175/BAMS-D-13-00290.1.

Bigg, E. K. (1953), The supercooling of water, *Proc. Phys. Soc. London*, *B66*, 688–694, doi:10.1088/0370-1301/66/8/309.

de Boer, G., H. Morrison, M. D. Shupe, and R. Hildner (2011), Evidence of liquid dependent ice nucleation in high-latitude stratiform clouds from surface remote sensors, *Geophys. Res. Lett.*, *38*(1), L01803, doi:10.1029/2010GL046016.

Brown, P. R. A., and P. N. Francis (1995), Improved Measurements of the Ice Water Content in Cirrus Using a Total-Water Probe, *J. Atmos. Ocean. Technol.*, *12*(2), 410–414, doi:10.1175/1520-0426(1995)012<0410:IMOTIW>2.0.CO;2.

Chen, F., and J. Dudhia (2001), Coupling an Advanced Land Surface–Hydrology Model with the Penn State–NCAR MM5 Modeling System. Part I: Model Implementation and Sensitivity, *Mon. Weather Rev.*, *129*(4), 569–585, doi:10.1175/1520-0493(2001)129<0569:CAALSH>2.0.CO;2.

Chen, T., W. B. Rossow, and Y. Zhang (2000), Radiative Effects of Cloud-Type Variations, *J. Clim.*, *13*(1), 264–286, doi:10.1175/1520-0442(2000)013<0264:REOCTV>2.0.CO;2.

Cooper, W. A. (1986), Ice Initiation in Natural Clouds, *Precip. Enhanc. Sci. Challenge, Meteor. Monogr., No. 43,*, Amer. Meteor. Soc., 29–32, doi:10.1007/978-1-935704-17-1_4.

DeMott, P. J. et al. (2011), Resurgence in Ice Nuclei Measurement Research, *Bull. Am. Meteorol. Soc.*, *92*(12), 1623–1635, doi:10.1175/2011BAMS3119.1.

Diao, M., M. A. Zondlo, A. J. Heymsfield, S. P. Beaton, and D. C. Rogers (2013), Evolution of ice crystal regions on the microscale based on in situ observations, *Geophys. Res. Lett.*, *40*(13), 3473–3478, doi:10.1002/grl.50665.

Diao, M., M. A. Zondlo, A. J. Heymsfield, L. M. Avallone, M. E. Paige, S. P. Beaton, T. Campos, and D. C. Rogers (2014), Cloud-scale ice-supersaturated regions spatially correlate with high water vapor heterogeneities, *Atmos. Chem. Phys.*, *14*(5), 2639–2656, doi:10.5194/acp-14-2639-2014.

Diao, M., J. B. Jensen, L. L. Pan, C. R. Homeyer, S. Honomichl, J. F. Bresch, and A. Bansemer (2015), Distributions of ice supersaturation and ice crystals from airborne observations in relation to upper tropospheric dynamical boundaries, *J. Geophys. Res. Atmos.*, *120*(10), 5101–5121, doi:10.1002/2015JD023139.

Diao, M., G. H. Bryan, H. Morrison, and J. B. Jensen. Ice nucleation parameterization and relative humidity distribution in idealized squall line simulations, submitted.

Dudhia, J. (1989), Numerical Study of Convection Observed during the Winter Monsoon Experiment Using a Mesoscale Two-Dimensional Model, *J. Atmos. Sci.*, *46*(20), 3077–3107, doi:10.1175/1520-0469(1989)046<3077:NSOCOD>2.0.CO;2.

Eidhammer, T., P. J. DeMott, and S. M. Kreidenweis (2009), A comparison of heterogeneous ice nucleation parameterizations using a parcel model framework, *J. Geophys. Res.*, *114*(D6), D06202, doi:10.1029/2008JD011095.

Ferrier, B. S. (1994), A Double-Moment Multiple-Phase Four-Class Bulk Ice Scheme. Part I: Description, *J. Atmos. Sci.*, *51*(2), 249–280, doi:10.1175/1520-0469(1994)051<0249:ADMMPF>2.0.CO;2.

Flatau, P. J., R. L. Walko, and W. R. Cotton (1992), Polynomial Fits to Saturation Vapor Pressure, *J. Appl. Meteorol.*, *31*(12), 1507–1513, doi:10.1175/1520-0450(1992)031<1507:PFTSVP>2.0.CO;2.

Gierens, K. (2003), On the transition between heterogeneous and homogeneous freezing, *Atmos. Chem. Phys.*, *3*, 437–446, doi:10.5194/acp-3-437-2003.

Gierens, K., U. Schumann, M. Helten, H. Smit, and A. Marenco (1999), A distribution law for relative humidity in the upper troposphere and lower stratosphere derived from three years of MOZAIC measurements, *Ann. Geophys.*, *17*(9), 1218–1226, doi:10.1007/s00585-999-1218-7.

Harrington, J. Y., M. P. Meyers, R. L. Walko, and W. R. Cotton (1995), Parameterization of Ice Crystal Conversion Processes Due to Vapor Deposition for Mesoscale Models Using Double-Moment Basis Functions. Part I: Basic Formulation and Parcel Model Results, *J. Atmos. Sci.*, *52*(23), 4344–4366, doi:10.1175/1520-0469(1995)052<4344:POICCP>2.0.CO;2.

Harrington, J. Y., D. Lamb, and R. Carver (2009), Parameterization of surface kinetic effects for bulk microphysical models: Influences on simulated cirrus dynamics and structure, *J. Geophys. Res.*, *114*(D6), D06212, doi:10.1029/2008JD011050.

Heymsfield, A. J. (1977), Precipitation Development in Stratiform Ice Clouds: A Microphysical and Dynamical Study, *J. Atmos. Sci.*, *34*(2), 367–381, doi:10.1175/1520-0469(1977)034<0367:PDISIC>2.0.CO;2.

Heymsfield, A. J., and L. M. Miloshevich (1995), Relative Humidity and Temperature Influences on Cirrus Formation and Evolution: Observations from Wave Clouds and FIRE II, *J. Atmos. Sci.*, *52*(23), 4302–4326, doi:10.1175/1520-0469(1995)052<4302:RHATIO>2.0.CO;2.

Heymsfield, A. J., L. M. Miloshevich, C. Twohy, G. Sachse, and S. Oltmans (1998), Upper-tropospheric relative humidity observations and implications for cirrus ice nucleation, *Geophys. Res. Lett.*, *25*(9), 1343–1346, doi:10.1029/98GL01089.

Heymsfield, A. J., L. M. Miloshevich, C. Schmitt, A. Bansemer, C. Twohy, M. R. Poellot, A. Fridlind, and H. Gerber (2005), Homogeneous Ice Nucleation in Subtropical and Tropical

Convection and Its Influence on Cirrus Anvil Microphysics, *J. Atmos. Sci.*, *62*(1), 41–64, doi:10.1175/JAS-3360.1.

Janjić, Z. I. (1994), The Step-Mountain Eta Coordinate Model: Further Developments of the Convection, Viscous Sublayer, and Turbulence Closure Schemes, *Mon. Weather Rev.*, *122*(5), 927–945, doi:10.1175/1520-0493(1994)122<0927:TSMECM>2.0.CO;2.

Jensen, E. J. et al. (2009), On the importance of small ice crystals in tropical anvil cirrus, *Atmos. Chem. Phys.*, *9*(15), 5519–5537, doi:10.5194/acp-9-5519-2009.

Kain, J. S. (2004), The Kain–Fritsch Convective Parameterization: An Update, *J. Appl. Meteorol.*, *43*(1), 170–181, doi:10.1175/1520-0450(2004)043<0170:TKCPAU>2.0.CO;2.

Kärcher, B. (2012), Supersaturation Fluctuations in Cirrus Clouds Driven by Colored Noise, *J. Atmos. Sci.*, *69*(2), 435–443, doi:10.1175/JAS-D-11-0151.1.

Kärcher, B., and W. Haag (2004), Factors controlling upper tropospheric relative humidity, *Ann. Geophys.*, *22*(3), 705–715, doi:10.5194/angeo-22-705-2004.

Koop, T., B. Luo, A. Tsias, and T. Peter (2000), Water activity as the determinant for homogeneous ice nucleation in aqueous solutions, *Nature*, *406*(6796), 611–4, doi:10.1038/35020537.

Korolev, A., E. Emery, and K. Creelman (2013), Modification and Tests of Particle Probe Tips to Mitigate Effects of Ice Shattering, *J. Atmos. Ocean. Technol.*, *30*(4), 690–708, doi:10.1175/JTECH-D-12-00142.1.

Korolev, A. V., and I. P. Mazin (2003), Supersaturation of Water Vapor in Clouds, *J. Atmos. Sci.*, *60*(24), 2957–2974, doi:10.1175/1520-0469(2003)060<2957:SOWVIC>2.0.CO;2.

Krämer, M. et al. (2009), Ice supersaturations and cirrus cloud crystal numbers, *Atmos. Chem. Phys.*, *9*(11), 3505–3522, doi:10.5194/acp-9-3505-2009.

Krämer, M. et al. (2016), A microphysics guide to cirrus clouds – Part 1: Cirrus types, *Atmos. Chem. Phys.*, *16*(5), 3463–3483, doi:10.5194/acp-16-3463-2016.

Liou, K.-N. (1986), Influence of Cirrus Clouds on Weather and Climate Processes: A Global Perspective, *Mon. Weather Rev.*, *114*(6), 1167–1199, doi:10.1175/1520-0493(1986)114<1167:IOCCOW>2.0.CO;2.

Mlawer, E. J., S. J. Taubman, P. D. Brown, M. J. Iacono, and S. A. Clough (1997), Radiative transfer for inhomogeneous atmospheres: RRTM, a validated correlated-k model for the longwave, *J. Geophys. Res. Atmos.*, *102*(D14), 16663–16682, doi:10.1029/97JD00237.

Morrison, H., G. Thompson, and V. Tatarskii (2009), Impact of Cloud Microphysics on the Development of Trailing Stratiform Precipitation in a Simulated Squall Line: Comparison of One- and Two-Moment Schemes, *Mon. Weather Rev.*, *137*(3), 991–1007, doi:10.1175/2008MWR2556.1.

Muhlbauer, A., T. P. Ackerman, J. M. Comstock, G. S. Diskin, S. M. Evans, R. P. Lawson, and R. T. Marchand (2014), Impact of large-scale dynamics on the microphysical properties of midlatitude cirrus, *J. Geophys. Res. Atmos.*, *119*(7), 3976–3996, doi:10.1002/2013JD020035.

Murphy, D. M., and T. Koop (2005), Review of the vapour pressures of ice and supercooled water for atmospheric applications, *Q. J. R. Meteorol. Soc.*, *131*(608), 1539–1565, doi:10.1256/qj.04.94.

Ovarlez, J., J.-F. Gayet, K. Gierens, J. Ström, H. Ovarlez, F. Auriol, R. Busen, and U. Schumann (2002), Water vapour measurements inside cirrus clouds in Northern and Southern hemispheres during INCA, *Geophys. Res. Lett.*, *29*(16), 60–1–60–4, doi:10.1029/2001GL014440.

Peter, T., C. Marcolli, P. Spichtinger, T. Corti, M. B. Baker, and T. Koop (2006), When dry air is too humid., *Science*, *314*(5804), 1399–402, doi:10.1126/science.1135199.

Phillips, V. T. J., P. J. DeMott, C. Andronache, V. T. J. Phillips, P. J. DeMott, and C. Andronache (2008), An Empirical Parameterization of Heterogeneous Ice Nucleation for Multiple Chemical Species of Aerosol, *J. Atmos. Sci.*, *65*, 2757–2783, doi:10.1175/2007JAS2546.1.

Pruppacher, H. R., and J. D. Klett (1996), *Microphysics of Clouds and Precipitation*, Atmospheric and Oceanographic Sciences Library, Springer Netherlands.

Reisner, J., R. M. Rasmussen, and R. T. Bruintjes (1998), Explicit forecasting of supercooled liquid water in winter storms using the MM5 mesoscale model, *Q. J. R. Meteorol. Soc.*, *124*(548), 1071–1107, doi:10.1002/qj.49712454804.

Sheridan, L. M., J. Y. Harrington, D. Lamb, K. Sulia, L. M. Sheridan, J. Y. Harrington, D. Lamb, and K. Sulia (2009), Influence of ice crystal aspect ratio on the evolution of ice size spectra during vapor depositional growth, *J. Atmos. Sci.*, *66*(12), 3732–3743, doi:10.1175/2009JAS3113.1.

Spichtinger, P., K. Gierens, U. Leiterer, and H. Dier (2003), Ice supersaturation in the tropopause region over Lindenberg, Germany, *Meteorol. Zeitschrift*, *12*(3), 143–156, doi:10.1127/0941-2948/2003/0012-0143.

Spichtinger, P., K. Gierens, and H. Wernli (2005a), A case study on the formation and evolution of ice supersaturation in the vicinity of a warm conveyor belt's outflow region, *Atmos. Chem. Phys.*, *5*, 973–987.

Spichtinger, P., K. Gierens, and A. Dörnbrack (2005b), Formation of ice supersaturation by mesoscale gravity waves, *Atmos. Chem. Phys.*, *5*(5), 1243–1255, doi:10.5194/acp-5-1243-2005.

Srivastava, R. C., and J. L. Coen (1992), New Explicit Equations for the Accurate Calculation of the Growth and Evaporation of Hydrometeors by the Diffusion of Water Vapor, *J. Atmos. Sci.*, *49*(17), 1643–1651, doi:10.1175/1520-0469(1992)049<1643:NEEFTA>2.0.CO;2.

Thompson, G., and T. Eidhammer (2014), A Study of Aerosol Impacts on Clouds and Precipitation Development in a Large Winter Cyclone, *J. Atmos. Sci.*, *71*(10), 3636–3658, doi:10.1175/JAS-D-13-0305.1.

Thompson, G., P. R. Field, R. M. Rasmussen, and W. D. Hall (2008), Explicit Forecasts of

Winter Precipitation Using an Improved Bulk Microphysics Scheme. Part II: Implementation of a New Snow Parameterization, *Mon. Weather Rev.*, *136*(12), 5095–5115, doi:10.1175/2008MWR2387.1.

Wylie, D. P., and W. P. Menzel (1999), Eight Years of High Cloud Statistics Using HIRS, *J. Clim.*, *12*(1), 170–184, doi:10.1175/1520-0442(1999)012<0170:EYOHCS>2.0.CO;2.

Zhang, C., and J. Y. Harrington (2015), The Effects of Surface Kinetics on Crystal Growth and Homogeneous Freezing in Parcel Simulations of Cirrus, *J. Atmos. Sci.*, *72*(8), 2929–2946, doi:10.1175/JAS-D-14-0285.1.

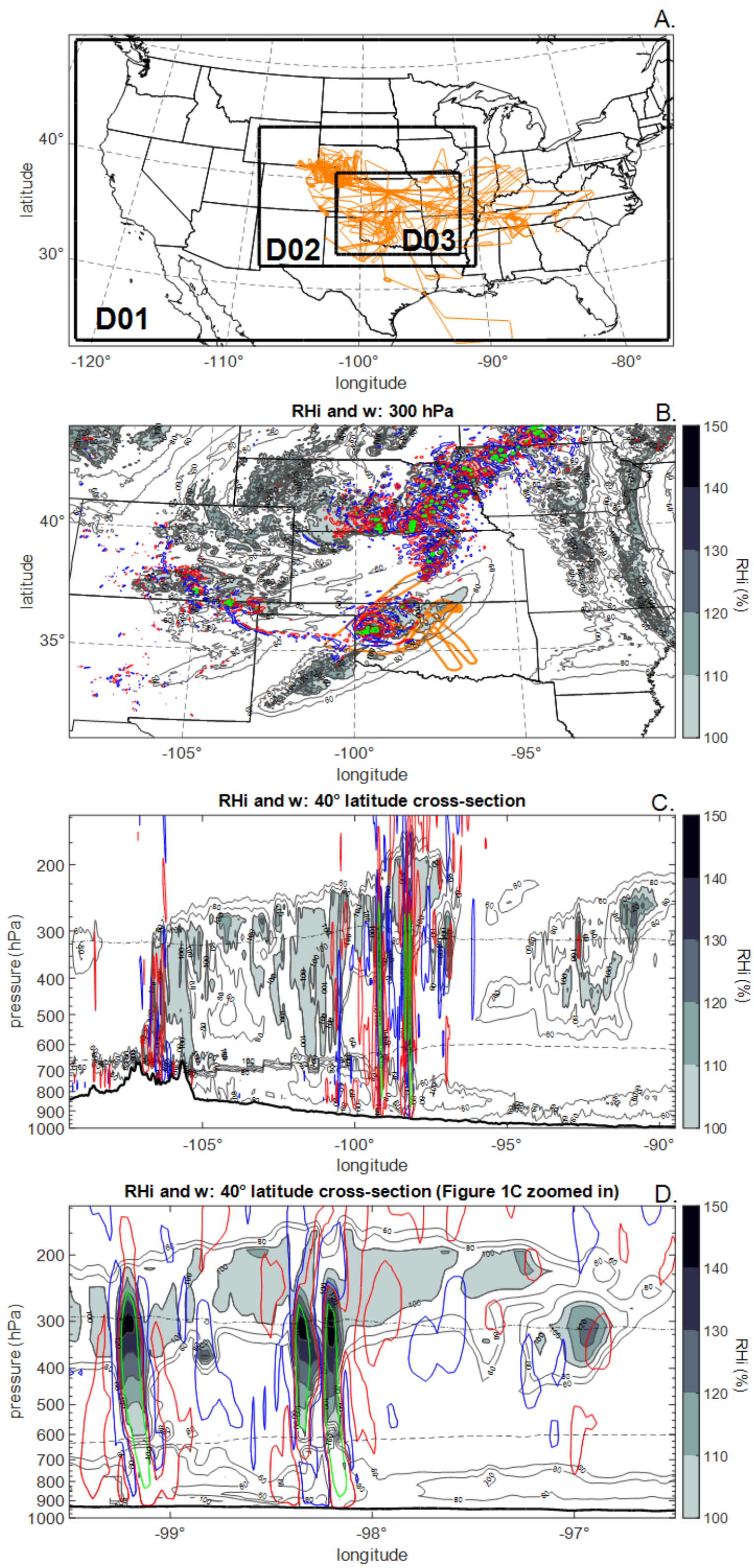

Figure 1: (A) The parent and nested domains for WRF simulations with all flight tracks from DC3 (thin orange lines). Distributions of RHi and vertical velocity in a horizontal cross section at

300 hPa (B) and in a vertical cross section at 40°N latitude (C and D), based on Thompson with the 2.4 km nested domain on May 20th, 2012 at UTC 0000. The May 19th flight track (thick orange line) is shown in Figure 1 B. Gray contours show RHi gradient, with shaded gray colors representing ice supersaturated regions. Vertical velocity contours are shown for -0.5 m s^{-1} (blue), +0.5 m s^{-1} (red), and ±5 m s^{-1} (green). The dashed and dot-dashed lines are the 0°C and -40°C isotherms, respectively.

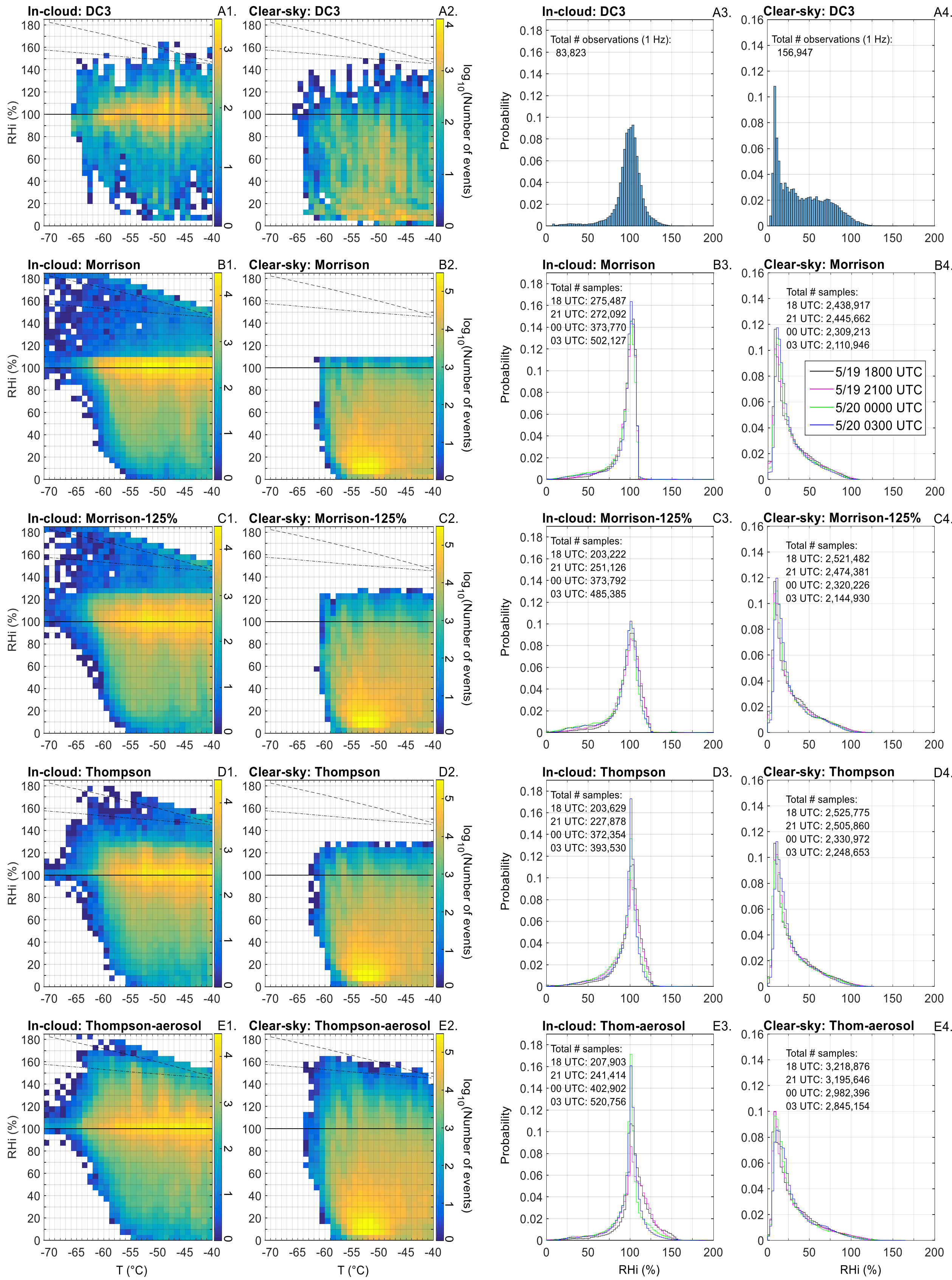
In-cloud: DC3
A1.
Clear-sky: DC3
A2.
In-cloud: DC3
A3.
Total # observations (1 Hz):
83,823
Clear-sky: DC3
A4.
Total # observations (1 Hz):
156,947
In-cloud: Morrison
B1.
Clear-sky: Morrison
B2.
In-cloud: Morrison
B3.
Total # samples:
18 UTC: 275,487
21 UTC: 272,092
00 UTC: 373,770
03 UTC: 502,127
Clear-sky: Morrison
B4.
Total # samples:
18 UTC: 2,438,917
21 UTC: 2,445,662
00 UTC: 2,309,213
03 UTC: 2,110,946
5/19 1800 UTC
5/19 2100 UTC
5/20 0000 UTC
5/20 0300 UTC
In-cloud: Morrison-125%
C1.
Clear-sky: Morrison-125%
C2.
In-cloud: Morrison-125%
C3.
Total # samples:
18 UTC: 203,222
21 UTC: 251,126
00 UTC: 373,792
03 UTC: 485,385
Clear-sky: Morrison-125%
C4.
Total # samples:
18 UTC: 2,521,482
21 UTC: 2,474,381
00 UTC: 2,320,226
03 UTC: 2,144,930
In-cloud: Thompson
D1.
Clear-sky: Thompson
D2.
In-cloud: Thompson
D3.
Total # samples:
18 UTC: 203,629
21 UTC: 227,878
00 UTC: 372,354
03 UTC: 393,530
Clear-sky: Thompson
D4.
Total # samples:
18 UTC: 2,525,775
21 UTC: 2,505,860
00 UTC: 2,330,972
03 UTC: 2,248,653
In-cloud: Thompson-aerosol
E1.
Clear-sky: Thompson-aerosol
E2.
In-cloud: Thom-aerosol
E3.
Total # samples:
18 UTC: 207,903
21 UTC: 241,414
00 UTC: 402,902
03 UTC: 520,756
Clear-sky: Thom-aerosol
E4.
Total # samples:
18 UTC: 3,218,876
21 UTC: 3,195,646
00 UTC: 2,982,396
03 UTC: 2,845,154
RHi (%)
T (°C)
log10(Number of events)
Probability

Figure 2: Occurrences of RHi with respect to temperature (two columns on the left) and probability density functions (PDFs) of RHi (two columns on the right) for DC3, Morrison, Morrison-125%, Thompson, and Thompson-aerosol. The comparisons for in-cloud and clear-sky conditions are shown separately. The RHi – T distributions are based on the composite of four time outputs from WRF simulations, with RHi and T binned by 5% and 1 K, respectively. The PDFs of RHi show these four WRF time outputs individually in different colored lines, with RHi binned by 2.5%. A total of 22 flights from DC3 are used in all the observation analysis. In the RHi – T distributions, the solid and dashed lines represent the saturations with respect to ice and with respect to liquid water calculated based on Murphy and Koop [2005], respectively. The homogeneous freezing line (dot-dashed) is based on Koop et al. [2000] with deliquesced particles at the diameters of 0.5 μm.

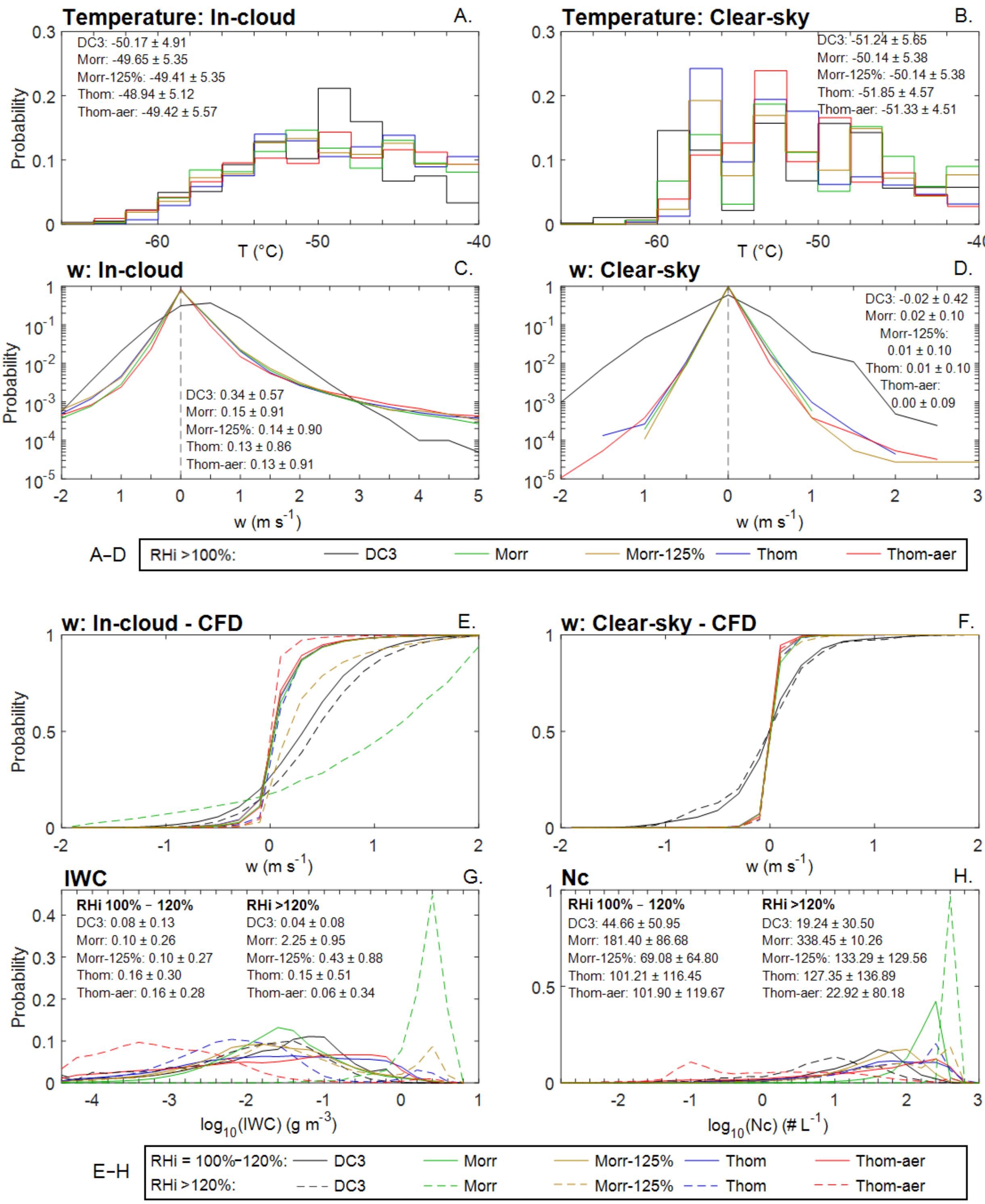

Figure 3: Normalized frequency distributions of temperature, w, IWC, and Nc for various ranges of ISS. Distributions of temperature and w are provided for in-cloud and clear-sky conditions (A–D). Cumulative Frequency Distributions (CFDs) of w are also provided for in-cloud and clear-sky conditions (E & F). Normalized frequency distributions of temperature, IWC, Nc, and

w are binned by 2°C, 0.2 g m^{-3}, 0.2 L^{-1}, and 0.5 m s^{-1}, respectively. The CFDs of w are restricted to ±2 m s^{-1} and are binned by 0.2 m s^{-1}. In A – D, solid color lines represent RHi > 100% for various datasets. In E – H, solid and dashed lines represent RHi = 100% – 120% and RHi > 120%, respectively. The mean and standard deviation (±σ) of each variable are provided in their respective figures. We note that the means and standard deviations for in-cloud and clear-sky w are calculated over the entire distribution of their respective datasets.

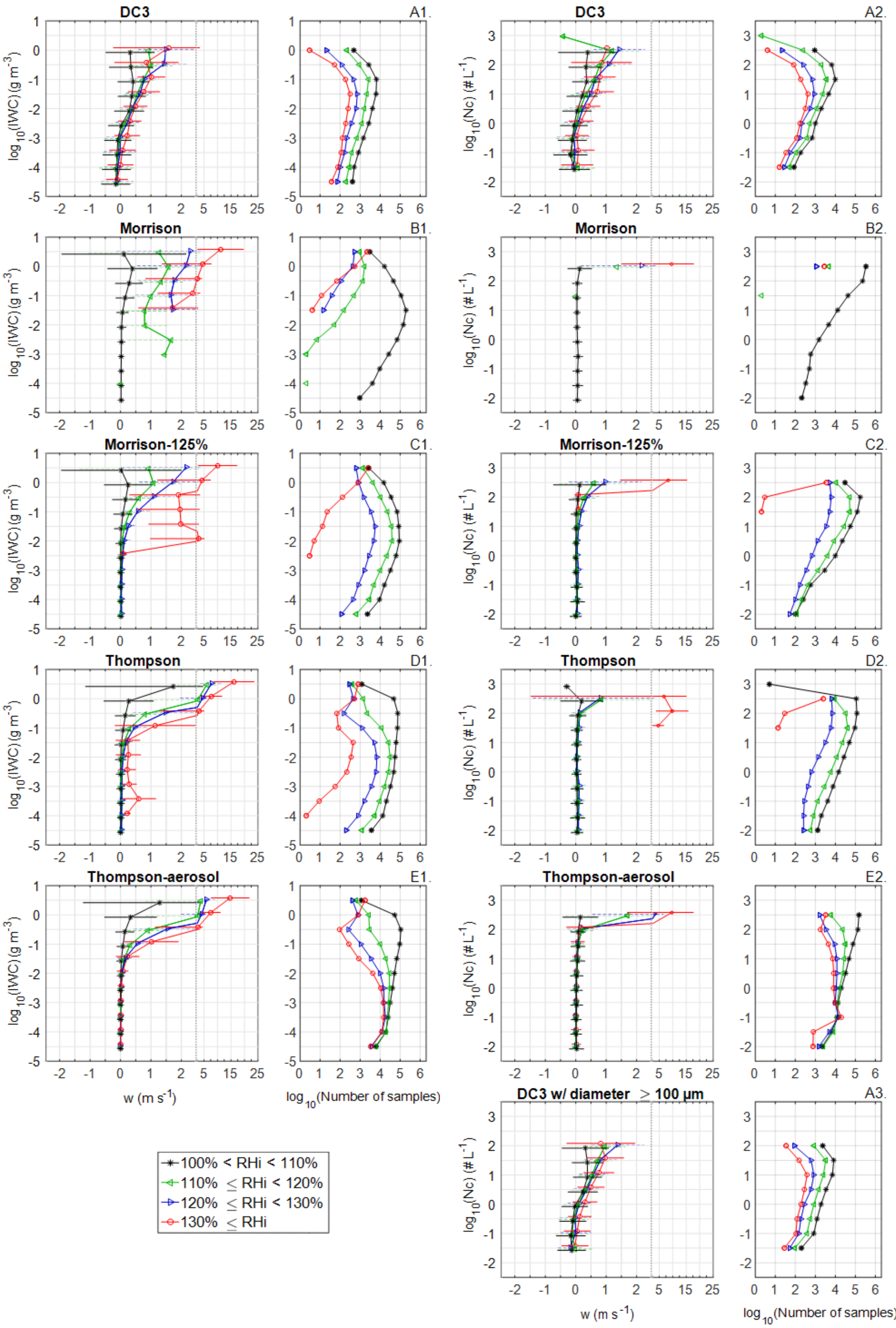

Figure 4: Average vertical velocity (w) binned by IWC (left two columns) and Nc (right two columns) for different ranges of ISS. Four ranges of ISS are shown in different colored lines. We

note that in order to show the different color lines clearly, we slightly shifted them vertically from each other, even though they are binned into the same ranges of IWC and Nc. Horizontal lines represent ±1 σ of the w in each bin, and the gray dashed lines highlight various ranges of w. The total number of samples is shown in the second and fourth columns. To illustrate the relatively small impacts from potential ice particle shattering in measurements, results with Nc observations excluding smaller ice particles (< 100 μm) are also shown in panel A3.

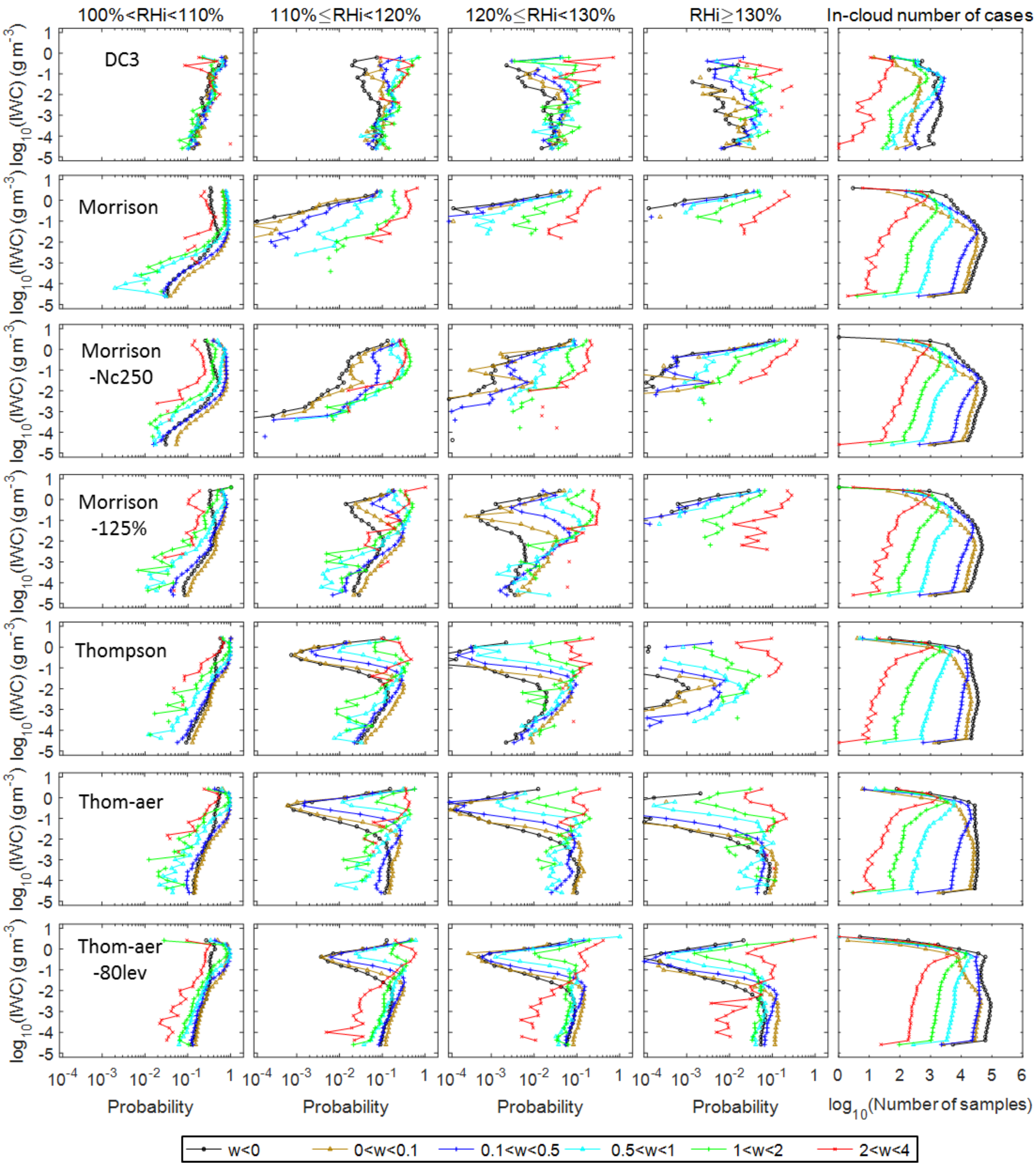

Figure 5: Probabilities of different magnitudes of ISS occurring at various ranges of w (shown in different colored lines), controlling for the IWC on the y-axis. The probability of a given range of ISS occurring is determined by normalizing the number of ISS occurrences in a certain ISS interval at a given range of w and IWC with the total number of occurrences of all RHi at that same range of w and IWC. Probabilities of ISS are shown in the logarithmic scale.

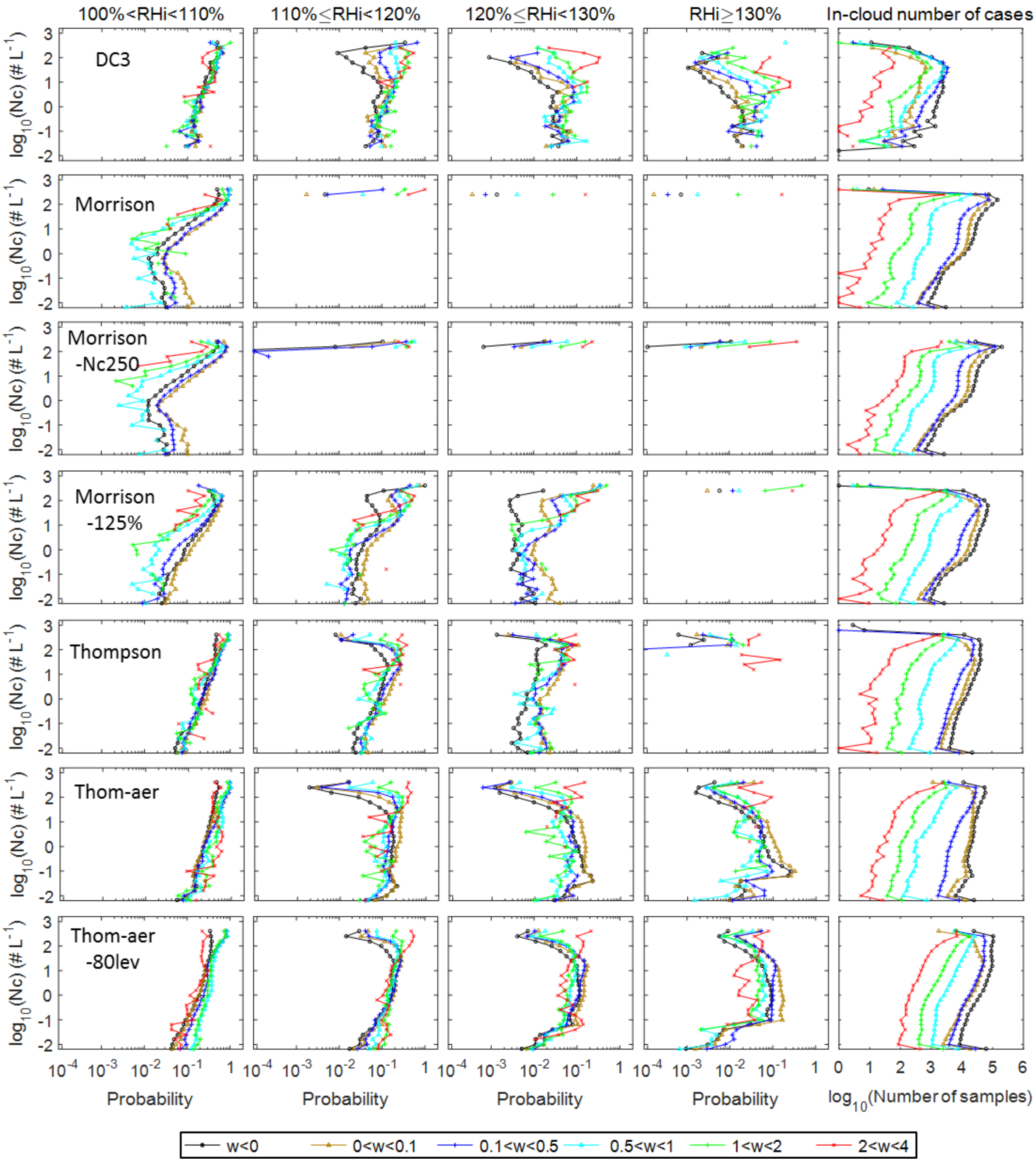

Figure 6: Similar to Figure 5, but controlling for Nc when analyzing the probabilities of different magnitudes of ISS occurring at various ranges of w. The factor of Nc is controlled on the y-axis.

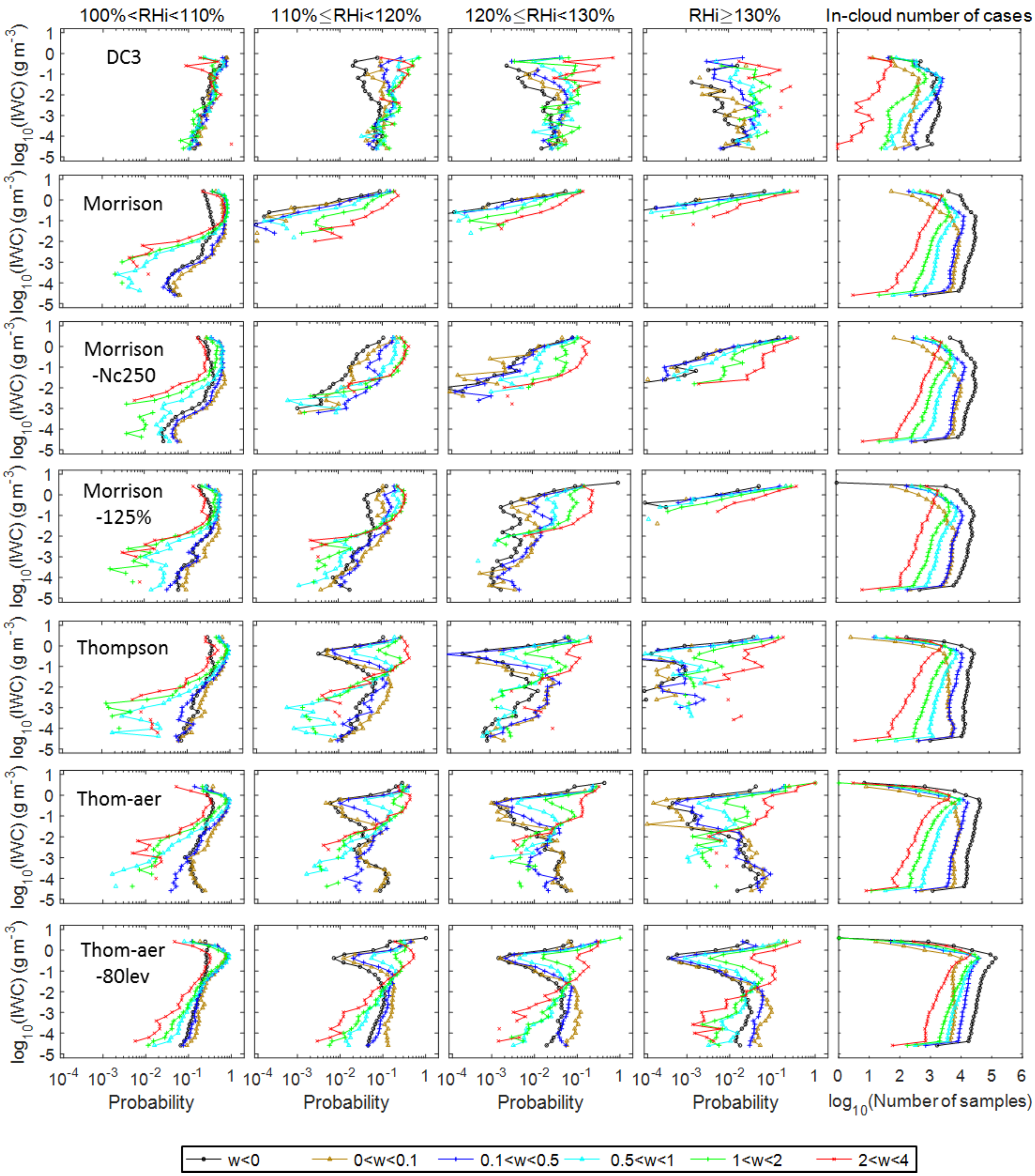

Figure 7: Same as Figure 5, except for using gridded data in a nested domain from higher resolution WRF simulations, i.e., at 800 m horizontal grid spacing. In this figure, the WRF datasets consist of gridded data from one time output: 20 May 2012 at UTC 0000.

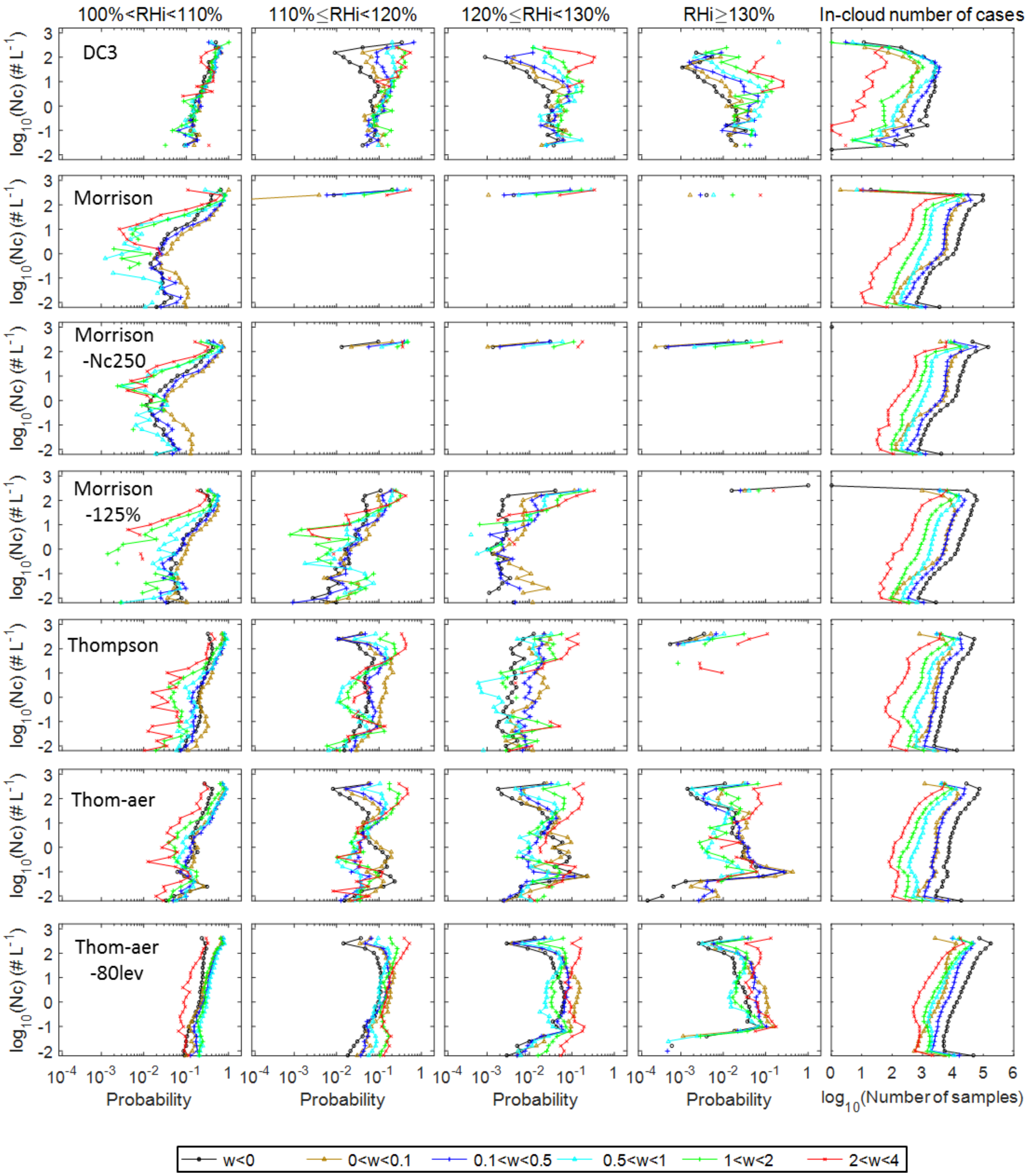

Figure 8: Same as Figure 6, except for using WRF simulations with 800 m horizontal grid spacing. In this figure, the WRF datasets consist of gridded data from one time output: 20 May 2012 at UTC 0000.

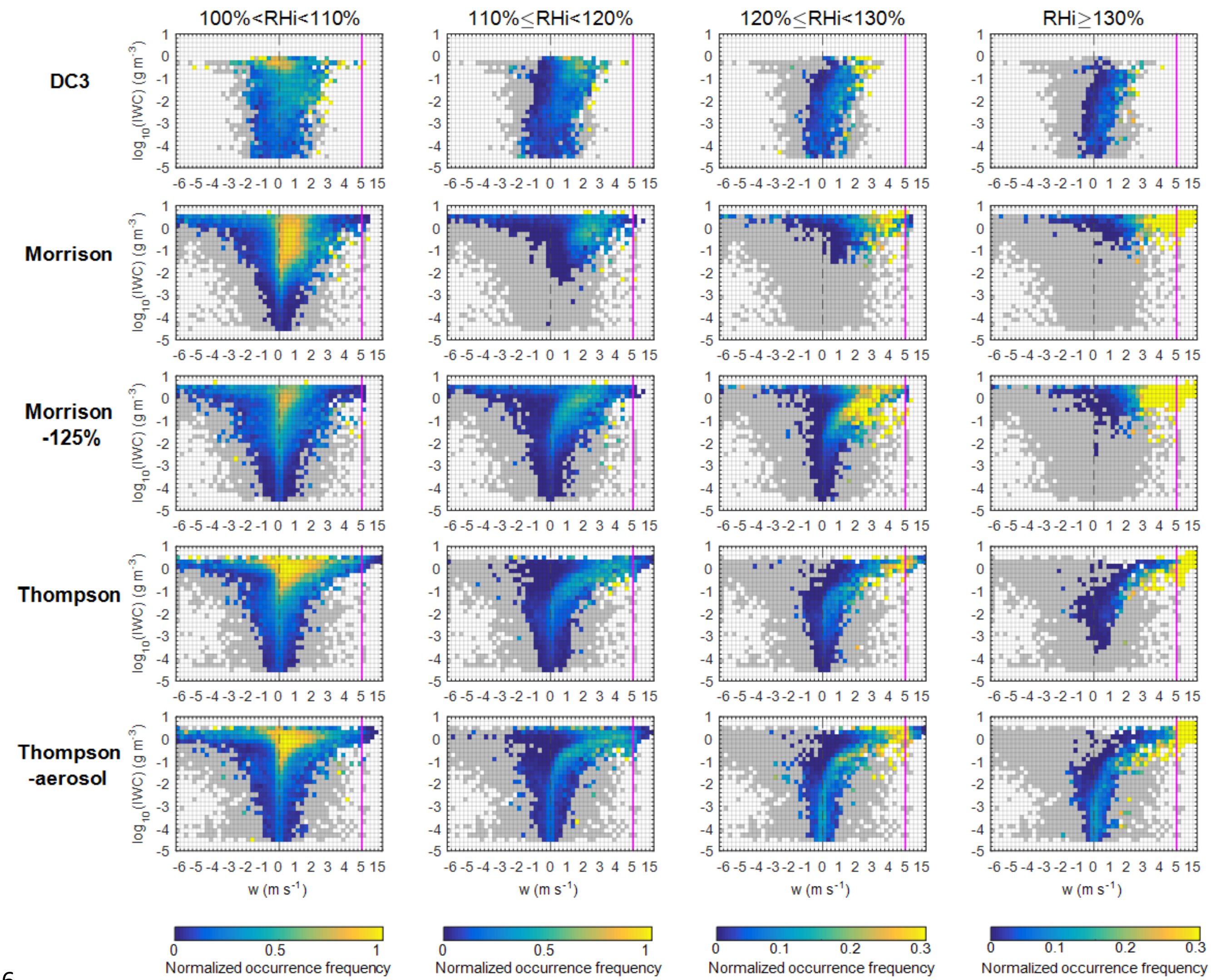

Figure 9: Normalized occurrence frequencies of ISS in relation to various magnitudes of w, controlling for IWC on the y-axis. The four columns show analyses at four different ISS intervals. Occurrence frequencies of ISS are calculated by normalizing the ISS occurrences at each w and IWC bin with the total number of occurrences of all RHi in that bin. We note that two different bin sizes of w are used here: w is binned by 0.25 m s^{-1} for w < 5 m s^{-1}, and by 2.5 m s^{-1} for w > 5 m s^{-1} (the maroon line highlights the transition between the two bin sizes). When w is below -6 m s^{-1} or greater than 15 m s^{-1}, these strong downdrafts/updrafts are grouped into the minimum and maximum w bins, respectively. The dashed line differentiates between updrafts and downdrafts. Gray colors represent the background of all RHi being observed or simulated.

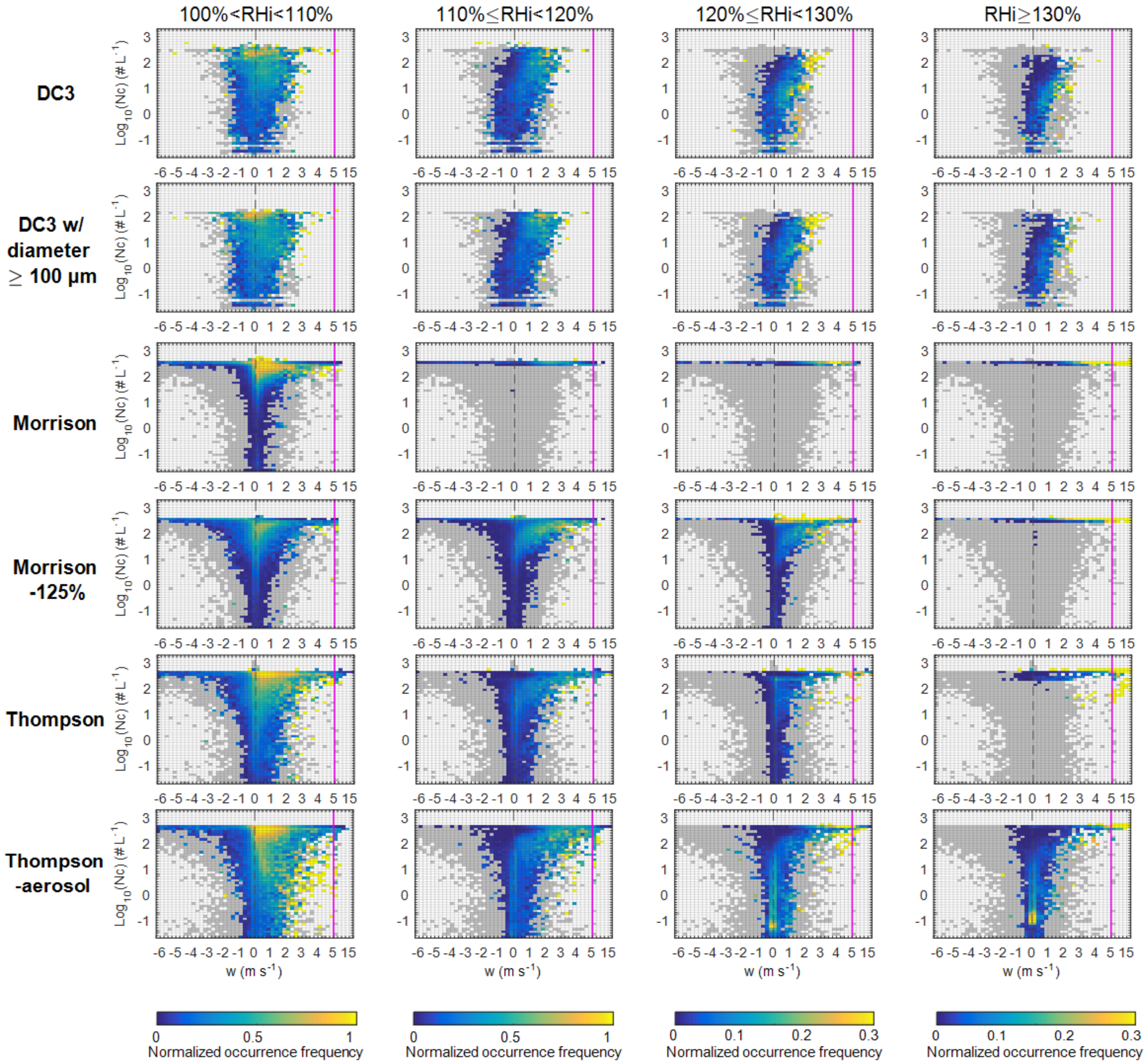

Figure 10: Same as Figure 9, except controlling for Nc when analyzing the correlations between ISS occurrence frequencies and w. To limit the potential ice shattering effects on the in-situ measurements, results that exclude ice particles smaller than 100 μm in DC3 dataset are shown in the second row.

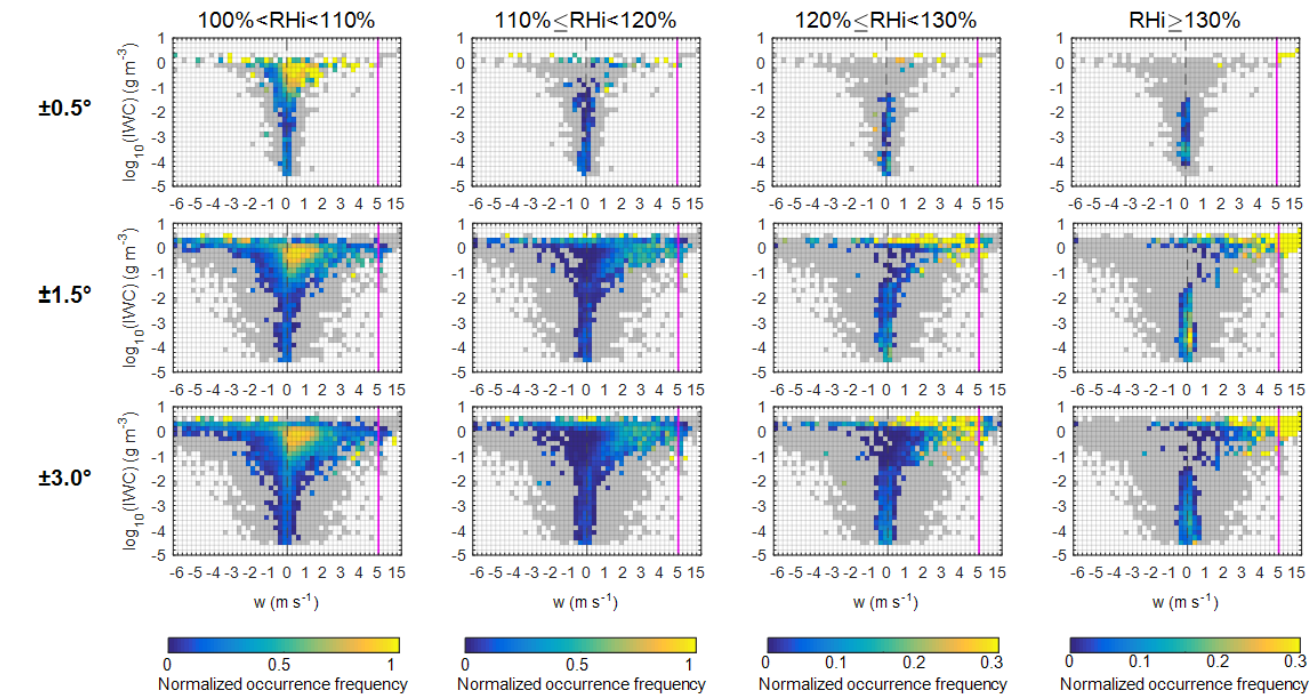

100%<RHi<110%
110%≤RHi<120%
120%≤RHi<130%
RHi≥130%
±0.5°
±1.5°
±3.0°
log10(IWC) (g m-3)
w (m s-1)
Normalized occurrence frequency

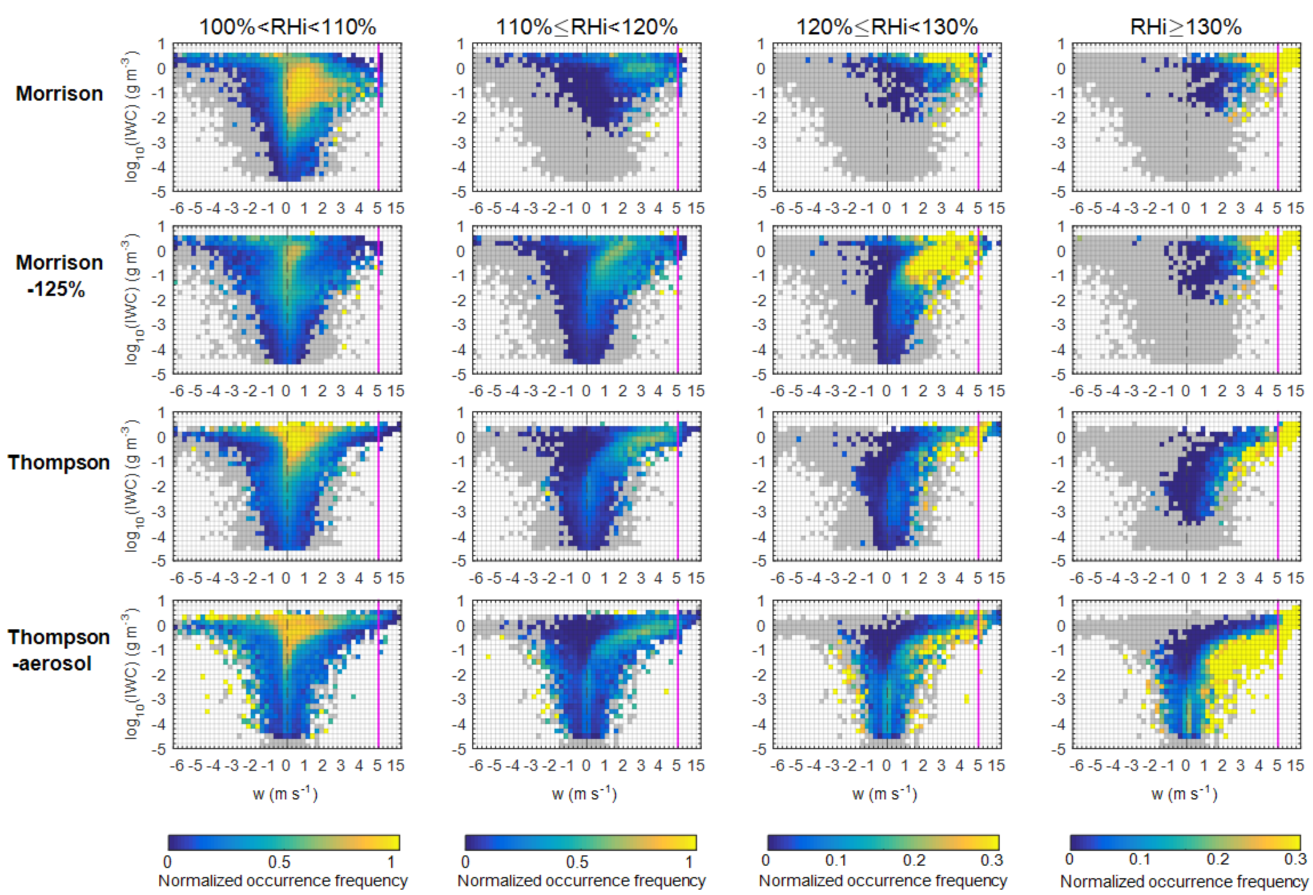

100%<RHi<110%
110%≤RHi<120%
120%≤RHi<130%
RHi≥130%
Morrison
Morrison -125%
Thompson
Thompson -aerosol
log10(IWC) (g m-3)
w (m s-1)
Normalized occurrence frequency

862

Figure 11: Similar to Figure 9, except for (top 3 rows) gridded data from Thompson-aerosol collocated with the May 19th GV aircraft observations within ±0.5°, ±1.5° and ±3.0° in latitude and longitude and within ±30 min; (bottom 4 rows) a different time period, i.e., during 11–12 June 2012 consisting of three merged time outputs (UTC 1600, 2000, and 0000).

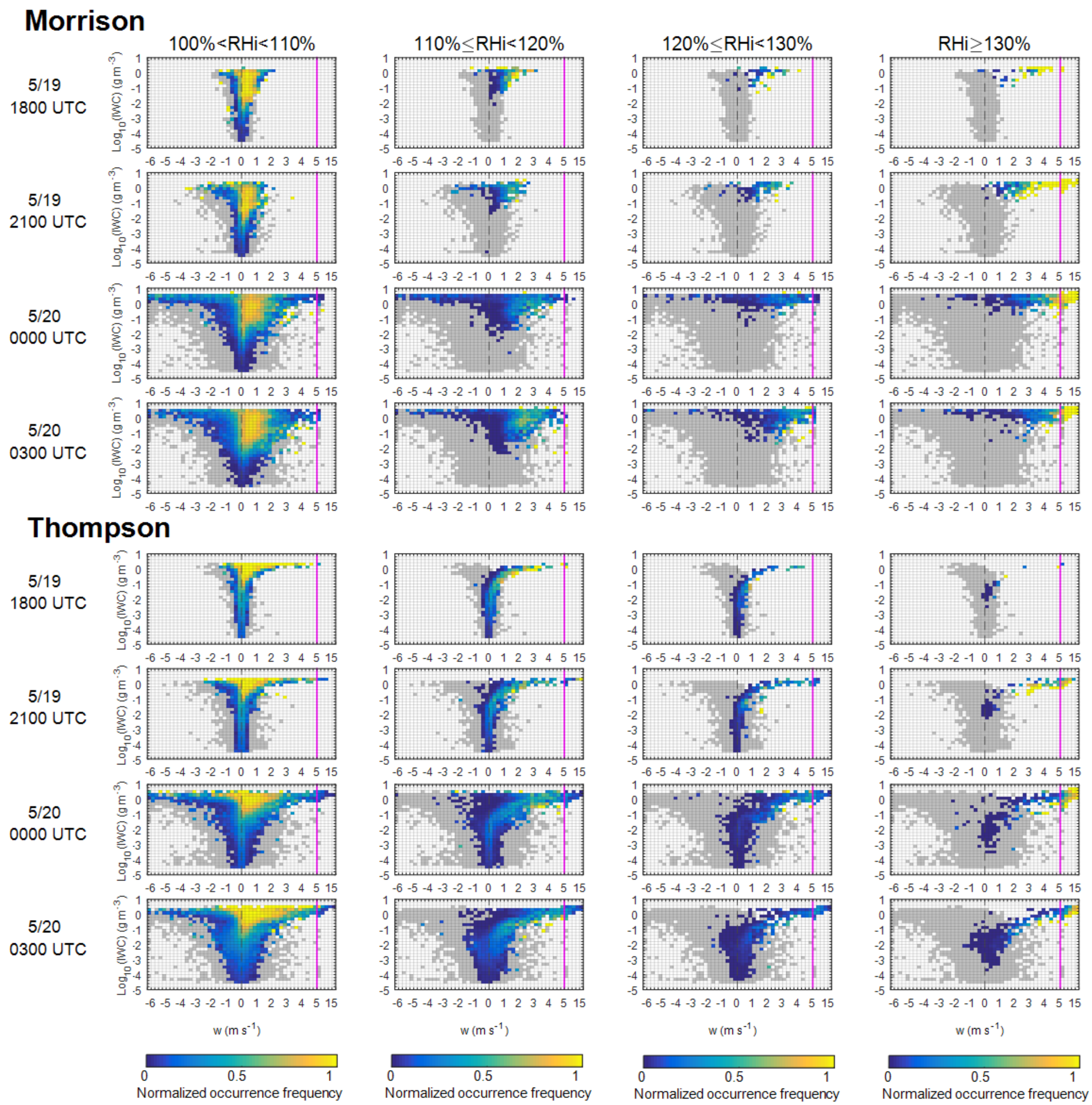

Figure 12: Similar to Figure 9, but shows four individual time outputs of WRF simulations at UTC 1800, 2100, 0000, 0300 during 19–20 May 2012. Results of the Morrison and Thompson simulations are shown in the top and bottom panels, respectively.